JPRS-CST-90-009
6 APRIL 1990

JPRS Report

Science & Technology

China

JPRS-CST-90-009
6 APRIL 1990

SCIENCE & TECHNOLOGY

CHINA

CONTENTS

Long March-4 Guidance, Attitude-Control, Trajectory Tracking & Measurement System

90CF0229 Beijing YUHANG XUEBAO [JOURNAL OF CHINESE SOCIETY OF ASTRONAUTICS] in Chinese No 4, Oct 89 (manuscript received 25 May 89) pp 3-9

[Article by Xu Xinhua [1776 0207 5478], Shao Zaimin [6730 6528 3046], Chen Baichu [7115 4102 0443], Guo Fang [6753 2397] of Research Institute 8, Ministry of Aeronautics and Astronautics Industry]

[Text] **Introduction**

The Long March-4 [CZ-4] is a three-stage launch vehicle which uses normal-temperature propellants. The rocket is 41.9 m long, and has a diameter of 3.35 m for its first and second stages and 2.9 m for the third stage; its lift-off mass is approximately 240 tons. The guidance system uses a platform/computer design, and the attitude-control system has a digital design. The first and second stages use a unidirectional-wobble servomechanism and the third stage uses a bidirectional wobble servomechanism. The control torque after third-stage engine cut-off is provided by anhydrous-hydrazine jet nozzles. The launch vehicle is equipped with continuous-wave responders, pulse responders and a set of laser reflectors which, in conjunction with the ground tracking and control station, constitute the trajectory tracking and measurement [TTM] system. The design of the guidance, attitude-control and TTM systems has been verified by flight test results.

The Guidance and Attitude-Control System

The guidance system uses a platform/computer design. Its main function is to control the launch vehicle to fly along a predetermined trajectory; to issue an engine cut-off command for each stage; and to issue lateral and normal steering commands during second-stage and third-stage flight for attitude control. The attitude-control system uses a platform/differential network/swivel-engine design. The operations of [detection] filtering, differential networking, switching control and signal synthesis are performed by an onboard computer; therefore, the attitude-control system is a digital control system. The main function of the attitude-control system is to maintain stable flight attitude. The main components of these two systems are the three-axis gyrostabilized platform, the onboard digital computer, the rate gyros, the

detection power amplifiers and the servomechanisms. The block diagrams of the two systems are shown in Figures 1 and 2, respectively. In Figure 1, N_{cx} are pitch pulse commands issued by the onboard computer which drive the mechanism inside the platform to execute the programmed pitch turn; N_{cp} are pulse commands issued by the onboard computer to drive the power distributor to continuously generate flight-sequence commands; $\dot{W}_x, \dot{W}_y, \dot{W}_z$ are, respectively, the output pulses of the three accelerometers located inside the platform. These final three pulses, which represent the apparent acceleration of the rocket, are received by the onboard computer where they are integrated and used in the engine cut-off equation to generate engine cut-off commands which are sent to the engine of each stage and to the terminal-velocity correction engine. In Figure 2, $\Delta U_\varphi, U_\psi, U_\gamma$ are, respectively, signals of the pitch, yaw, and roll angles measured by the platform; and $U_{\dot{\varphi}}, U_{\dot{\psi}}, U_{\dot{\gamma}}$ are, respectively, signals of the attitude angular rates measured by the rate gyros. They are all signals with a 1,000 Hz a.c. carrier. The signals are detection filtered and converted into slowly-varying d.c. signals; then they are sampled in the onboard computer, A/D converted, and used in the difference-equation calculations. At the same time, the integrated acceleration outputs are used to generate lateral and normal steering commands. The two signals are synthesized, and D/A converted in the onboard computer. The synthesized signal is then sent to the detection power amplifier which controls the servomechanism to drive the swivel engines. After third-stage engine cut-off and prior to satellite-rocket separation, the onboard computer executes a switching logic discrimination program which, through the switching amplifier, controls the opening and closing of the electromagnetic valves in the anhydrous-hydrazine jet nozzles to accomplish attitude control.

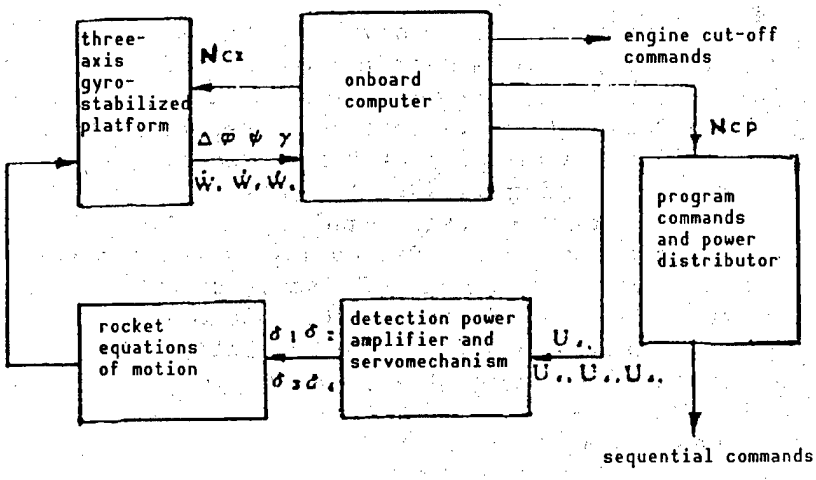

Figure 1. Block Diagram of Guidance System

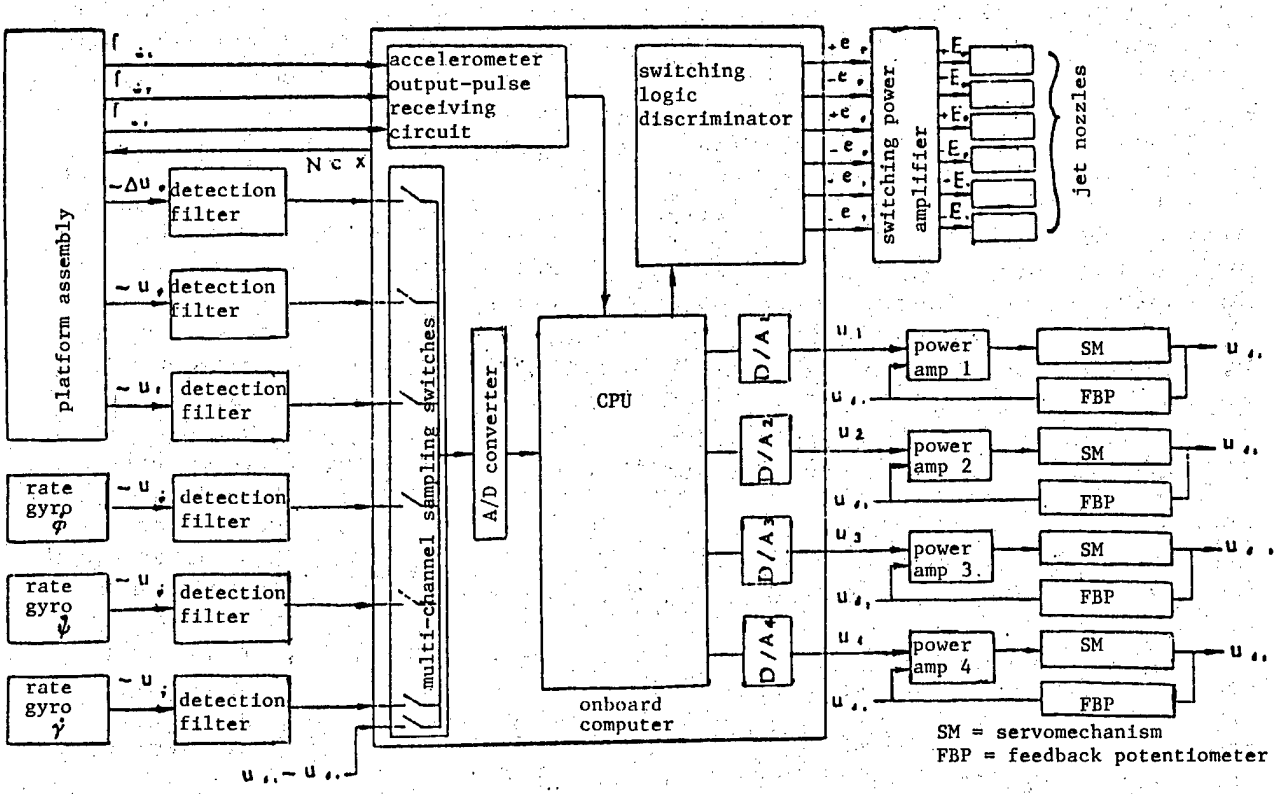

Figure 2. Block Diagram of Attitude-Control System

In order to reduce the number of onboard devices, the detection filter and the power amplifier are combined into a single unit called the detection power amplifier. The power supply for the detection power amplifier is contained within the unit. The A/D and D/A converters are integral parts of the onboard computer. Effective design measures are used to protect against interference. For example, the computer housing is isolated from the rocket body, and is connected to the zero line of the power supply. At the computer input and output, where long cables are required, decoupling capacitors are installed to eliminate sharp disturbances. At the signal input and output ports, measures are taken to isolate the transformers, the photoelectric couplers and circuits. The signal transmission cables are generally shielded by grounding and by connecting to the zero line of the power supply.

Operation of the Guidance System

The Engine Cut-Off Equation

The engine cut-off equation for the first, second and third stages is as follows:

$$\Delta W_i = \overline{W}_i - [W_{xi} + k_{i2}W_{yi} + k_{i3}W_{zi} + k_{i4}\dot{W}_{xi} + k_{i5}\dot{W}_{yi} + k_{i6}\dot{W}_{zi} + k_{i7}\ddot{W}_{xi} + k_{i8}\ddot{W}_{yi} + k_{i9}\ddot{W}_{zi} + k_{i10}\dddot{W}_{xi} + k_{i11}\dddot{W}_{yi} + k_{i12}\dddot{W}_{zi} + f_i(\Delta t)]$$

where $\overline{W}_i$ is the built-in characteristic velocity of the ith-stage engine cut-off equation;

k_{i2}, k_{i3}, ⋯ ⋯, k_{i12} are the coefficients of the engine cut-off equation;
W_x, W_y, W_z are the apparent velocity components in the gravity inertial coordinate system;
$\dot{W}_x$, $\dot{W}_y$, $\dot{W}_z$ are the first integrals of the apparent velocity components;
$\ddot{W}_x$, $\ddot{W}_y$, $\ddot{W}_z$ are the second integrals of the apparent velocity components;
$\dddot{W}_x$, $\dddot{W}_y$, $\dddot{W}_z$ are the third integrals of the apparent velocity components;
and $f_i(\Delta t)$ is the time-compensation function of the ith-stage engine cut-off equation.

The onboard computer continuously calculates the value inside the bracket of the above equation and compares it against the built-in value $\overline{W}_i$; when $(\Delta)W_i$ reaches zero, an engine cut-off command is issued.

The above engine cut-off equation greatly simplifies computation because it avoids the complex process of solving the navigation equation using the accelerometer-output method; rather it uses the integrals of the accelerometer output directly to compute the engine cut-off commands. By linearizing the navigation equation about the predetermined launch trajectory, and applying the concept of a pulse-transition function based on the linearized variable-coefficient system (the pulse-transition function is the inverse Laplace transform of the transfer function, also called the system power function), it is possible to establish an integral expression between the apparent acceleration and the velocity and position of the rocket. By substituting these expressions into the engine cut-off equation (expressed in terms of the rocket velocity and position), the above engine cut-off equation can be derived.

The Steering Equation

Steering is accomplished by a closed-loop control system. It applies linear control theory to form steering commands in the pitch and yaw channels based on differences between the apparent velocity obtained from the measured accelerometer output and the apparent velocity of the predetermined flight trajectory. These commands are synthesized with the attitude-control signals inside the onboard computer and sent to the detection power amplifier. There is no steering during first-stage flight.

The steering equation is as follows:

$$u_\psi(\psi) = K_{i1}\delta W_x + K_{i2}\delta W_y + K_{i3}\delta W_z + K_{i4}\delta \dot{W}_x + K_{i5}\delta \dot{W}_y + K_{i6}\delta \dot{W}_z$$

where K_{i1}, K_{i2}, ⋯ ⋯, K_{i6} are the coefficients of the steering equation for the ith stage.

The coefficients of the steering equation can be either constants or variables or piecewise constants, depending on the characteristics of the launch trajectory, the steering parameters and the required steering effect.

Operation of the Attitude-Control System

The operation of the attitude-control system is illustrated in Figure 3. The output of the controlled object x(t) is measured by the sensing element and sent to the onboard computer. x(t) is a continuous variable which is sampled periodically by the sampling switch of the onboard computer to produce a discrete signal $x^*(t)$. The pulse-transfer function of the computer is denoted by $D^*(s)$; its output $y^*(t)$ is also a discrete variable. The time lag for A/D conversion and for the computer operation can be represented by the loop e^{-*Ts}. After D/A conversion, the discrete variable $y^*(t)$ becomes a continuous variable y(t); this can be expressed mathematically by a zeroth-order holding device.

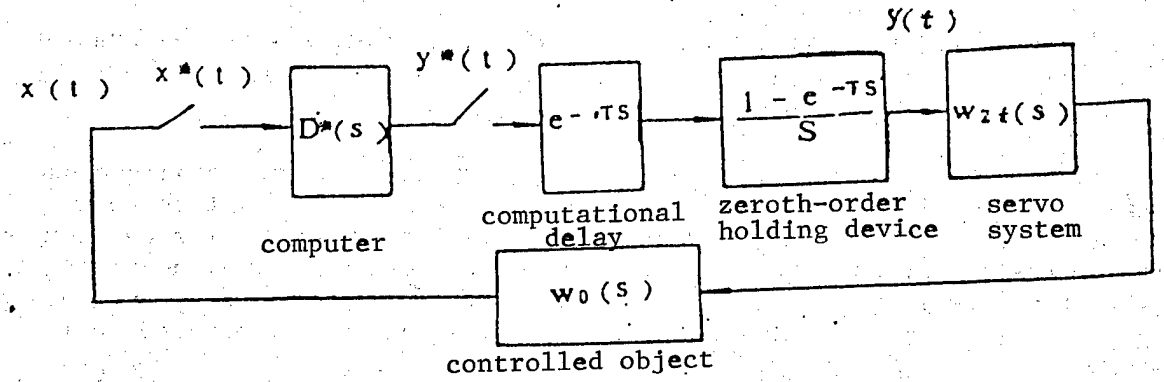

Figure 3. Digital Attitude-Control System

The characteristics of the digital correction network of the attitude-control system can be represented by the difference equation:

$$y(nT)=\frac{1}{b_0}\left[\sum_{k=0}^{m} a_k x(\overline{n-kT})-\sum_{k=1}^{m} b_k y(\overline{n-kT})\right]$$

where T is the sampling period (20 ms) and m is the order of the difference equation (no greater than 8). By using a serial planning technique, the 8th-order difference equation can be converted into two 4th-order networks connected in series; this eliminates the computational error caused by the built-in coefficients of the difference equation.

After third-stage engine cut-off, the attitude-control system follows the nonlinear control scheme as shown in Figure 4, where y_s is computed from the difference equation. The formulas used to realize the nonlinear control are as follows:

$$\begin{cases} y(nT)=0 & y_{s1}\geqslant y_s(nT)\geqslant -y_{s1} \\ y(nT)=y_c & y_s(nT)\geqslant y_{s2} \\ y(nT)=-y_c & y_s(nT)\leqslant -y_{s2} \\ y(nT)=\begin{cases} 0 \\ y_c \end{cases} & \begin{matrix} y_{s2}>y_s(nT)>y_{s1}, y(\overline{n-1T})\neq y_c \\ y_{s2}>y_s(nT)>y_{s1}, y(\overline{n-1T})=y_c \end{matrix} \\ y(nT)=\begin{cases} 0 \\ -y_c \end{cases} & \begin{matrix} -y_{s1}>y_s(nT)>-y_{s2}, y(\overline{n-1T})\neq -y_c \\ -y_{s1}>y_s(nT)>-y_{s2}, y(\overline{n-1T})=-y_c \end{matrix} \end{cases}$$

These discrimination formulas are used to control the opening and closing of the anhydrous-hydrazine nozzles, which in turn control the attitude of the vehicle.

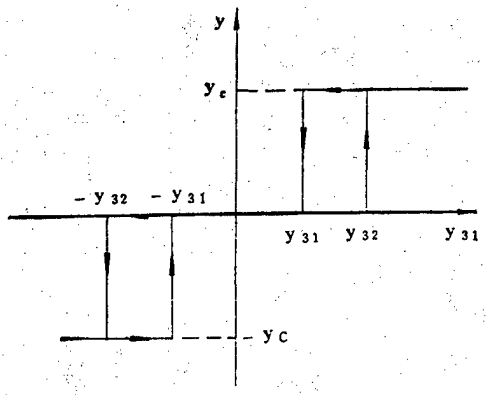

Figure 4. Control Law for Switching Logic

Onboard Computer

The onboard computer consists of the following components: the central processing unit (CPU), the main memory, the channel-control unit, the interface circuits, the adjusting unit and the secondary power supply; these components are connected by a dual-bus structure: a high-speed independent bus is used for information exchange between the CPU and internal memory units; a separate I/O bus is used for information exchange between the CPU and input/output. A block diagram of the onboard computer is shown in Figure 5.

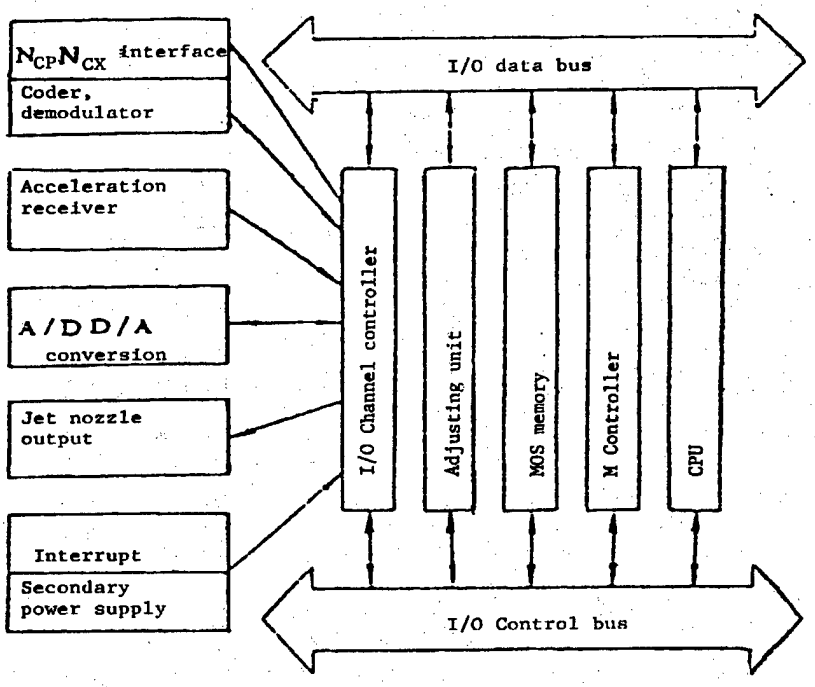

Figure 5. Block Diagram of Onboard Computer

The technical specifications of the onboard computer are:

Master frequency	4000 kHz
Word length	16 bits
Operating speed	addition/subtraction 3.25 μs multiplication 13 μs division 13.75 μs
Main memory capacity	4KB (semiconductor storage)
Mode of operation	single-length and double-length fixed-point operation
Channel commands	30; basic commands: 55
Interrupt levels	8 with program selective priority
Number of bits in A/D converter	11
A/D conversion speed	less than 2 ms
Sampling period	20 ms
Number of channels in sampling switch	22

The flight software is of modular design; it consists of the following programs: the main control program, a 1-ms interrupt processing program, the A/D-interrupt processing program, the telemetry-interrupt processing program and the output-channel interrupt processing program. The main control program and the interrupt processing programs at each stage are organically joined. The primary functions of the main control program are: to perform the integration of the apparent velocity and to compute the components of the engine cut-off equation to form millisecond increments. The primary functions of the 1-ms interrupt processing program are: to sample the output of the accelerometer, to perform the integration in order to form velocity increments, to compute the increments of the engine cut-off equation, to issue engine cut-off commands, to generate pitch program pulses and power-distributor drive pulses, and to issue A/D sampling commands to all channels at 4-ms intervals. The main functions of the A/D-interrupt processing program are: to acquire the A/D converted values from each channel, to carry out calculation of the difference equation, to perform signal synthesis and send the synthesized signal to the D/A output, and to perform switching-logic discrimination for controlling the opening and closing of the jet nozzles. A complete cycle of the above flight sequence operation takes 20 ms.

Trajectory Tracking and Measurement System

The main function of the TTM system is to perform real-time measurement and monitoring of the rocket trajectory by coordinating with the ground station. The system consists of two segments: the optical measurement segment and the radio measurement segment. The optical measurement system, which consists of three cine theodolites on the ground and an onboard laser reflector, performs close-range orbit measurements during first-stage flight. A continuous-wave (CW) measurement system, which consists of a three-channel CW interferometer and an onboard CW velocity and position responder, provides high-precision velocity and position information.

Located along the flight path of the launch vehicle are three monopulse radars which are linked to the onboard pulse responders to form a monopulse radar chain; they provide auxiliary information to the radio measurement system.

To facilitate ground acquisition and tracking of the launch vehicle, the ground station is equipped with a guidance unit which, in conjunction with the onboard beacon, constitutes the guidance system.

During the period from 60 seconds after launch to second-stage engine cut-off, the post-processing accuracy of the measurement system is:

$$\sigma_x = \sigma_y = \sigma_z < 10m$$
$$\sigma_{\dot{x}} = \sigma_{\dot{y}} = \sigma_{\dot{z}} < 0.05m/s$$

The characteristics of the CW responder are:

Operating frequency	C-band
Receiver sensitivity	-126 dBW
Dynamic range	-65 ~ -126 dBW
Acquisition time	0.1 sec
Separation between transmit and receive	40 dB
Accuracy	Random phase error $\sigma_{\varphi R} < 5°$, $\sigma_{\varphi 5MHz} < 0.5°$

The characteristics of the pulse responder are:

Operating frequency	C-band
Trigger sensitivity	-91 dBW
Transponder pulse parameter	width approximately 1 μs
Dynamic range	50 dB
Transponder pulse delay	Selectable
Delay stability	20 ns
Transponder frequency stability	1.5×10^{-11}/50 ms

The characteristics of the guidance beacon are:

Operating frequency	S-band
Frequency accuracy	4.25×10^{-8}
Frequency stability	4.7×10^{-8}
Clutter suppression	> 40 dB

The antenna of the responders and the beacon are installed flush with the rocket body. The gain patterns and polarizations of the antennas are designed by taking into consideration the ascending trajectory of the rocket and the locations and performance of the ground stations. The basic data of the antennas are listed in Table 1.

Table 1. Antenna Characteristics of the Onboard Responder

Name	Quantity	Frequency band	Polarization	Type
Beacon antenna	1	S	L	Microstrip
Pulse antenna	1	C	L	Microstrip
CW antenna	2	C	RHCP	Microstrip

Flight Test Results

Orbit-Injection Accuracy

The requirement for orbit-injection accuracy and the actual measured results are shown in Table 2.

Table 2. Satellite Orbit-Injection Accuracy

Parameter	Design specifications	Measured orbital value
Deviation in period ΔT	±12s	-5.2s
Deviation in eccentricity Δe	0.005	0.0024
Deviation in inclination ΔT	±0.12°	0.10°

Flight Attitude Angles and Steering Commands

The variation of flight-attitude angles and steering commands are shown in Figure 6 [not reproduced], where $t_{f1,2}$ is the time of separation of the first and second stages, $t_{f2,3}$ is the time of separation of the second and third stages, and t_{k3} is the time of third-stage engine cut-off.

During first-stage flight the maximum pitch angle of the rocket is 0.73°, the maximum yaw angle is -0.73°, and the maximum roll angle is 1.7°. The large roll angle is caused by the disturbance torque produced by the compression deformation of the first-stage engine mount under thrust. During second-stage flight, the maximum pitch angle is 2°, the maximum yaw angle is -4°, and the maximum roll angle is -1.5°. These attitude angles are the result of the combined actions of disturbances and steering. During third-stage flight, the maximum pitch angle is 6.33°, the maximum yaw angle is -1.6°, and the maximum roll angle is 0.88°. During the terminal-velocity correction stage, the maximum pitch angle is -1°, the maximum yaw angle is 0.54°, and the maximum

roll angle is 0.5°. The attitude angles during the entire flight are much smaller than the design specifications, which are 15° for maximum pitch and yaw and 5° for maximum roll.

At the time of satellite-rocket separation, the pitch angle is 0.22°, the yaw angle is 0.2°, and the roll angle is 0.33°. The deviations in attitude angles at orbit injection are very small.

The tracking and measurement system performed steady measurements of the rocket during its entire flight, with the CW responders maintaining continuous tracking, until satellite-rocket separation. At a slant range of 3,500 km, telemetry showed that the received voltage of the responder still had a 20 dB margin. Over a large portion of the trajectory, the pulse responder succeeded in triggering all three radar stations simultaneously. The measurement accuracy was higher than design specification.

References

1. Tion Chang Hsia, "A Technique for Synthesizing Digital Filter," IEEE TRANS. ON IBM, Vol IM-18, No 2, 1969, p 6.

2. Jutius, T. Tou, "Digital and Sampled-Data Control System," New York: McGraw-Hill Book Co., Inc., 1959.

Experimental Soft X-Ray Laser Research With Lithium-Like Si Ions

90CF0103A Shanghai ZHONGGUO JIGUANG [CHINESE JOURNAL OF LASERS] in Chinese Vol 16 No 10, Oct 89 p 616 [MS received 26 Sep 89]

[Article by Xu Zhizhan [1776 5267 1455], Fan Pinzhong [5400 0756 1813], Zhang Zhengquan [1728 2973 3123], Chen Shisheng [7115 2514 0524], Lin Lihuang [2651 4409 3552], Lu Peixiang [7120 1014 4382], Wang Xiaofang [3769 2556 2455], Qian Aidi [6929 1947 1229], and Yu Jiajin [0151 0502 6651] of the Shanghai Institute of Optics and Fine Mechanics, Chinese Academy of Sciences: "Experimental Study of Soft X-Ray Laser with Lithium-Like Silicon Ions"; see also earlier report in JPRS-CST-89-024, 1 Nov 89 p 16]

[Text] Based on obtaining some preliminary experimental results using the six-path laser apparatus at the Shanghai Institute of Optics and Fine Mechanics (SIOFM) of the Chinese Academy of Sciences, soft X-ray lasing corresponding to transition wavelengths of 8.89 nm and 8.73 nm was successfully achieved with complex pumping of Li-like Si ions using the LF-12# laser apparatus on 10-16 Aug 89.

In the soft X-ray gain experiment with Li-like Si ions using the LF-12# laser apparatus, the driving laser wavelength was 1.05 microns and the pulse width was approximately 0.9 ns. The laser energy on the target was 50 J (mean deviation < 15 percent). The output laser beam was focussed on a flat silicon target strip by a six-element cylindrical lens and aspheric lens system to produce a linear laser plasma in a high valance state to be used as the gain medium for the soft X-ray laser. The length of the line of focus was 20 mm and its width was approximately 130 microns. This corresponds to a focussed laser power density of approximately 2×10^{12} W/cm^2 on the target. A polished flat silicon surface was used in the experiment; its thickness was 1 mm. Changing the target width can result in a linear plasma gain medium of equal laser intensity but different length. The main diagnostic instrument was an XUV [extreme ultraviolet] high-resolution spectrograph, which was developed by this research group and is equipped with a grazing-incidence grating (2400 L/mm) for one-dimensional space resolution, and a pinhole-type X-ray transmission grating (2000 L/mm)

spectrograph. They were placed co-axially facing each other horizontally on either side of the focal line. Kodak 101-01 film, already calibrated for the system, was used for taking the X-ray spectra. A very clear XUV spectrum was obtained once the target was hit.

Using the stigmatic grazing-incidence grating spectrograph, we found that spontaneous emission due to 5f-3d (8.89 nm) and 5d-3p (8.73 nm) transitions of the lithium-like Si^{11+} ions was significantly amplified. The time integral of the axial XUV emission spectra was measured for linear plasmas of various lengths in the experiment. It was found that the intensity of these two transition lines increased exponentially with the length of the plasma. The gain coefficients were 1.5 cm^{-1} and 1.4 cm^{-1}, respectively. The products of maximum gain and length were 2.7 and 2.5, respectively. A spatial distribution of the spectral line gain at different locations from the target surface was also obtained using the spatial resolution characteristics of the spectrograph.

There has been no other report on the successful development of a soft X-ray laser with lithium-like silicon ions as described above. It is particularly significant that the two new lithium-like silicon-ion laser spectral lines, which are under 10 nm, were obtained at low laser power density. This indicates that our existing laser apparatus has great potential in the research of X-ray lasers.

This study was done with the support of Professors Wang Daheng [3769 1129 3801], Chen Nengkuan [7115 5174 1401], Deng Ximing [6772 6932 6900], and Yang Guozhen [2799 0948 2823] and the close cooperation of the operators of the LF-12# laser apparatus at SIOFM. In particular, the LF12# target provided us with a high-quality laser focussing system. The Kodak 101-01 film was supplied by Professor Schafer, Director of the FRG's Max Planck Institute for Biophysical Chemistry. The authors wish to express their gratitude to all these supporters and collaborators.

This subject was funded as a major project in the Chinese Academy of Sciences, by the National Natural Science Foundation, and also as a national high-technology project.

Single-Mode Nanosecond Double-Pulse Ruby Laser

90CF0103B Shanghai ZHONGGUO JIGUANG [CHINESE JOURNAL OF LASERS] in Chinese Vol 16 No 10, Oct 89 pp 619-620 [MS received 04 Feb 88]

[Article by Shen Jinhui [3088 2516 0565] and Qu Linjie [2575 2651 2638] of the Department of Precision Instruments, Tianjin University: "Single-Mode Nanosecond Double-Pulse Ruby Laser"]

[Text] Abstract

An in-situ shearing scheme is presented based on a Q-switched ruby laser.

Key Words: spark gap, double pulse, ruby laser.

A laser-triggered spark gap was used to trip an optical shutter in a conventional Q-switched ruby laser to produce two 1-ns-wide single-mode pulses in a single Q-switch process. The pulses are approximately 15 ns apart and the spacing can be easily adjusted based on demand.

I. Experimental Apparatus and Principle

The experimental apparatus is shown in Figure 1. The transmission line is energized with full-wave voltage V_λ. The spark gap is adjusted so that it almost breaks down at a static voltage $V_\lambda - V_{\lambda/4}$. When the thyratron voltage is lowered for Q-switching, an overvoltage is built up across the spark gap, which is higher than its breakdown voltage. When the Q-switched pulse is established inside the cavity, the light leaking from the side of the polarizer P triggers the spark gap. As a result of the intense electric field built up by the overvoltage and the energy of the light, the spark gap breaks down within a few nanoseconds, forming an electrically conductive channel with virtually no resistance. Thus, the high voltage V_λ stored in transmission line 1 is once again applied to the Q-switch crystal KD*P. As a result of impedance matching, the actual voltage wave form on the KD*P is a $V_{\lambda/2}$ square wave. Figure 2 shows this process. The width of this square wave is

determined by the length of the transmission line: $\Delta t = l/v$, where v is the speed at which the electrical signal is transmitted in the line.

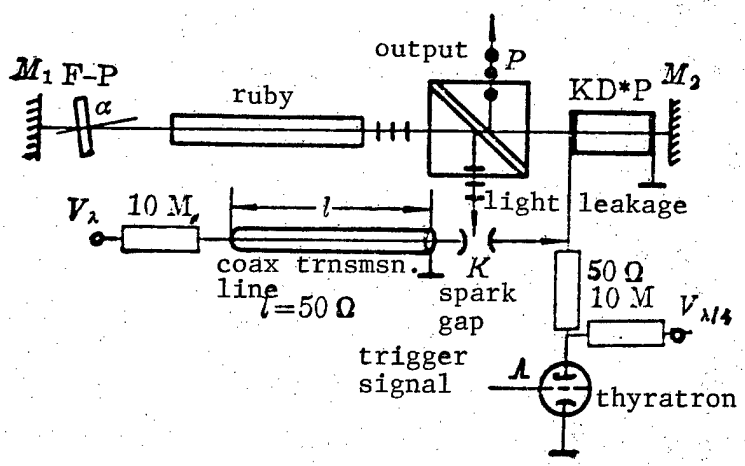

Figure 1. Schematic Diagram of the Experimental Set-Up: M1, M2 - reflective mirrors; P - Glan prism

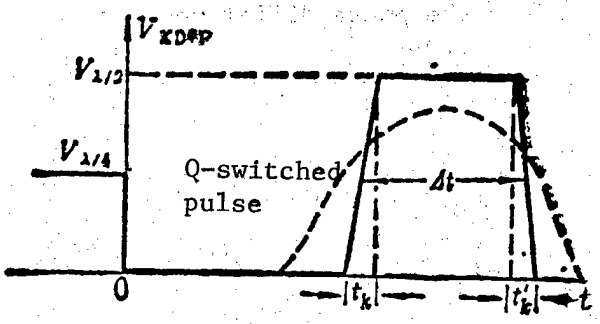

Figure 2. Voltage Variation of the Electro-Optical Crystal

Since the direction of polarization of the light inside the cavity is not affected by whether there is a voltage $V_{\lambda/2}$ applied to the electro-optical crystal, there is no light output at the Glan prism P. However, during the process whereby the voltage applied to the crystal rises from 0 to $V_{\lambda/2}$ or declines from $V_{\lambda/2}$ to 0, the polarization direction of the photon that passes through KD*P changes to produce an output. When the voltage is $V_{\lambda/4}$, the output reaches its maximum. Since the base width of the light pulse is equal to the width of the leading (or trailing) edge of the square wave, its half width is only half of the leading or trailing edge of the square wave.[1] As long as the width of the square wave is less than that of the Q-switched pulse width, it is possible to use the leading and trailing edge to shear two coherent light pulses in a single Q-switch process.

II. Spark-Gap Characteristics and Pulse-Width Analysis

It has been proven in theory and practice that there is a time delay, t_p, in the breakdown of a spark gap. The higher the overvoltage, the smaller t_p becomes. It ranges from several dozen ns to a few microseconds. Within this period, if it is triggered by a laser pulse at some energy level, the spark gap can rapidly break down in a few ns.

The conduction time of the spark gap, t_k, is determined by the widths of the leading and trailing edge of the $V_{\lambda/2}$ square wave. It is possible to determine t_k by solving the discharge circuit equation. Figure 3 shows the equivalent circuit. The approximate solution[2] is:

$$t_k = 21\frac{pd^2}{\alpha u_0^2} + 2.2\frac{L}{R}$$

when p is the gap pressure (atm), d is the electrode spacing (cm), α is the collision-ionization coefficient (atm.cm^2/s), u_0 is the voltage applied to the spark gap, L is the total inductance of the discharge circuit, and $R = \rho + R_L$ is the sum of the characteristic impedance of the coaxial cable and the load resistance. Based on Barson's (?) law, the breakdown voltage u is a monotropic function of (pd). When u_0 is a constant, an increase in the pressure p helps reduce t_k. In addition, the critical breakdown voltage is also dependent upon the shape of the electrodes and composition of the gas. Experimentally, we were able to obtain a 3.3-kV half-wave voltage square wave with a t_k = 2 ns leading edge.

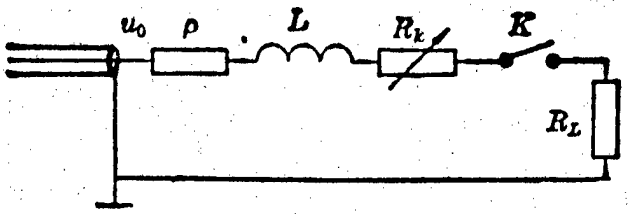

Figure 3. Equivalent Circuit of the Transmission-Line Discharge Circuit Through the Spark Gap; R_k - spark-gap resistance

III. Experimental Results and Analysis

Based on the requirement of dynamic holography, the interval between the two pulses was chosen to be Δt = 15 ns. The pulse interval depends on the width of the $V_{\lambda/2}$ square wave. It can be easily adjusted by varying the length of the transmission line. Because an electrical signal travels at 0.1 m/ns in the transmission line, the length of the transmission line was chosen to be l = 1.5 m.

Figure 4 shows the wave form of the two pulses. It was measured with a PIN detector with a response time of 800 ps and displayed with a 275-MHz-bandwidth Model 1727 storage oscilloscope. The pulse width is 1 ns and the spacing is 15 ns.

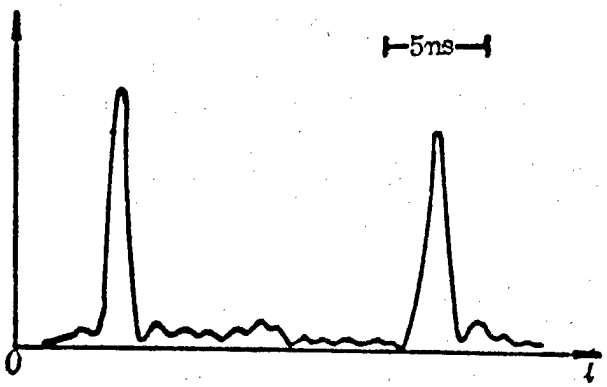

Figure 4. Wave Form of the Sheared Double Pulses

The optical length of the resonance cavity is 0.5 m. It takes a photon 3.3 ns to travel back and forth. After the Q-switched pulse is established, the entire 3.3 ns of optical path is evenly distributed with a large number of photons. The in-situ shearing process is to cut out two 1-ns-wide light pulses. Because the spatial distribution of photons becomes non-uniform after the first pulse is sheared from the cavity, it is necessary to slightly adjust the length of the transmission line to allow the trailing edge of the square wave to shear a large number of photons.

Because a high Q-switched pulse is only present inside the cavity for approximately 3.0 ns, it is necessary to fine-tune the trigger power of the spark gap (which is achieved by adjusting the spark gap). It makes conduction happen near the peak in the leading edge of the huge pulse and cuts out the first pulse. Thus, the trailing edge of the huge pulse has a larger adjustable range to cut out a second pulse more or less with the same magnitude as the first pulse. In holography and high-speed photography, there is little impact when the energy of the light exposure differs by half.

After two 1-ns-half-width pulses are taken away from the 3.3-ns optical path cavity, most of the energy inside the cavity is consumed. The peak power of each pulse is approximately equal to the peak power of the huge pulse inside the cavity. Since there are reflective mirrors on both ends, the peak power of the huge pulse formed inside the cavity is higher than the Q-switched peak output power near which is semi-reflective at one end.

In order to obtain single-mode output, a 3-mm-thick mode-selector etalon with a 15-percent reflectance was placed in the cavity. Since these two pulses are sheared from the same Q-switched pulse, they are both single mode and coherent. The output mode was determined with a 120-mm etalon and a single-mode light ring was observed.

References

1. D. Faubert, et al., OPT. AND LASER TECHNOLOGY, 2, 79 (1981).

2. T. A. Mischatz (?), "Generation of High-Power Nanosecond Pulses," (Atomic Energy Publishing House, Beijing, 1982), p 140.

Design of 10.6-Micron Glass-Metallic Complex-Waveguide Polarized Laser

90CF0103C Shanghai ZHONGGUO JIGUANG [CHINESE JOURNAL OF LASERS] in Chinese Vol 16 No 10, Oct 89 pp 623-624 [MS received 23 Dec 87]

[Article by Wang Ruifeng [3769 3843 1496] and Qiu Qi [6726 3825] of the Optoelectronics Technology Section, Chengdu Institute of Radio Engineering: "Design of a 10.6- μm Glass-Metal Complex Polarized Laser"]

[Text] Abstract

This paper presents a theoretical method for calculating the structural parameters of a glass-metal complex-waveguide polarized laser. General structural parameters of this type of laser are obtained. Corresponding to total lengths of 330 mm and 470 mm, output power levels of 7.5 W and 9 W, respectively, were obtained. More than 98 percent of the laser output is in a linearly polarized base mode.

Key Words: complex waveguide, polarization, 10.6 μm.

I. Introduction

Due to the development of infrared soft-metal waveguide technology in recent years, the CO_2 polarized laser has attracted widespread attention. Conventionally, a polarized laser is obtained with a Brewster window. The disadvantages include bulkiness, structural complexity, high cost, and difficulty in obtaining high-power output. To this end, we have proposed a CO_2 laser which is polarized by a glass-metal complex waveguide[1] and have experimentally proven its feasibility. In this paper, based on the mathematical method introduced by Abrams to analyze the propagation of the EH_{11} mode of a hollow dielectric waveguide outside the waveguide,[2] we derived the height of the metal plate waveguide during optimal coupling. The length and width of the plate waveguide were determined based on the transmission and loss characteristics of the metal-plate waveguide mode.

II. Structural Design

2.1 Height of the Metal-Plate Waveguide D

Figure 1 shows a schematic diagram of the laser. Since there is some free space between the circular waveguide and plane waveguide, the coupling between the two can be approximated as two parts, i.e., coupling between the circular waveguide and free space and coupling between free space and the plane waveguide. The circular hollow glass waveguide can easily estabish an oscillation in the EH_{11} mode.[3] Based on the method presented by Abrams,[2] for the Gaussian beam in the EH_{11} mode entering free space from the glass waveguide, the relation between the beam waist radius ω_0 and dielectric waveguide radius α can be approximately expressed as:

$$\omega_0 = 0.6435\,\alpha \qquad (1)$$

The beam waist is located at the end of the dielectric waveguide. Reference [4] derived the optimal coupling condition for a Gaussian beam entering a metal-plate waveguide. When

$$\eta=\frac{2\omega_0}{D}=0.7$$

we have

$$2\omega_0=0.7D \qquad (2)$$

At this time, the TE_{01} mode of the plane waveguide is most effectively excited; its excitation efficiency is greater than 98 percent. In order to minimize losses, spacings between the metal-plate waveguide and the circular glass waveguide and the plane mirror must be reduced to the extent possible in order to neglect the issue of dispersion of a Gaussian beam in free space. Substituting equation (1) into (2), one obtains the optimal coupling condition:

$$D=1.8386a=0.9193d \qquad (3)$$

where D is the height of the plate waveguide and d is the diameter of the dielectric waveguide.

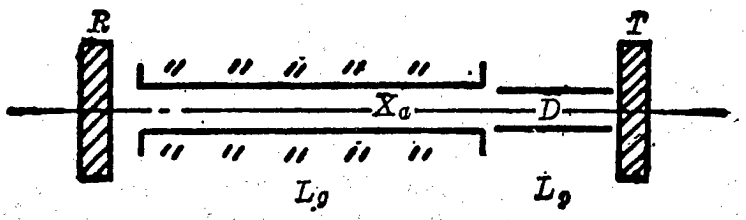

Figure 1. Structure of Laser

2.2 Length of the Metal-Plate Waveguide Lp

Theoretically, the length of the metal-plate waveguide ought to meet the following conditions: (1) one-way gain of the laser must be greater than its loss, (2) TM modes must be suppressed to have TE mode oscillation, (3) transmission coupling loss is minimum. The transmission loss of a metal-plate waveguide is very small. Usually, the loss coefficient $\alpha_{TE_{01}} \approx 10^{-7}\,cm^{-1}$, $\alpha_{TM_{01}} \approx 10^{-4}\,cm^{-1}$, and $\alpha_{EH_{11}} \approx 10^{-3}\,cm^{-1}$. In addition, $\alpha_{TE_{11}} / \alpha_{TM_{01}} \approx 10^{-3}$, therefore, TM modes can be suppressed to achieve oscillation in TE modes. Now, all that remains to be discussed is condition (3).

From Figure 1 we know that all modes travelling in the plane waveguide are reflected by the plane mirror to return to the circular waveguide entrance. Different orders of modes have different phase delays. The return field E'(y) is not the same as the field E(y), at the entrance of the circular waveguide. There is a coupling loss between the two. E(y) and E'(y) can be expressed as:

$$\left.\begin{aligned} E(y) &= e^{-y^2/\omega_0^2} = \sum_{l=0}^{\infty} A_l \cos(2l+1)\frac{\pi}{D}y \\ E'(y) &= \sum_{l=0}^{\infty} A_l \cos(2l+1)\frac{\pi}{D}y \cdot e^{i\phi_l} \end{aligned}\right\} \qquad (4)$$

In these equations, similar phase factors are eliminated. Thus, the plane-waveguide attenuation coeficient is neglected. The phase factor is expressed as

$$\phi_l = 2L_p\beta_l + \pi$$

where Lp is the length of the plane waveguide, π is an abrupt phase change, and β_l is the phase factor of the lth-order mode.[5] The coupling loss is

$$C = 1 - \left\{ \frac{\sum_{l,m} A_l^2 A_m^2 \cos 2L_p(\beta_l - \beta_m)}{\sum_{l,m} A_l^2 A_m^2} \right\}^{1/2} \qquad (5)$$

Numerical computation was done with a computer to obtain two curves for D = 3 mm and D = 3.2 mm at η = 0.7, as shown in Figure 2. The figure shows that loss in the metal-plate waveguide increases with length. However, in the range of 10 < Lp/D < 13, loss does not significantly vary with length. Usually, the distance between the mirror and the plasma tube entrance in an internal-cavity laser is required to be greater than 3 cm. Obviously, 10 < Lp/D < 13 is a rational range. In practice, we chose Lp = 10D.

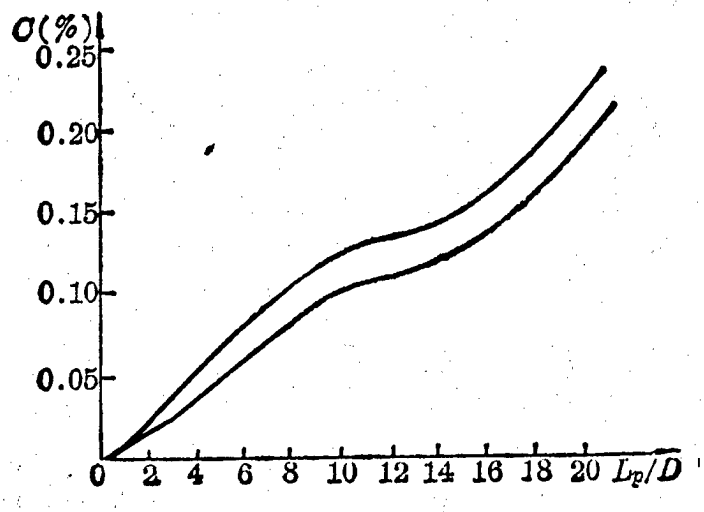

Figure 2. Metal-Plate Waveguide Loss Curves
upper curve: D = 3 mm, lower curve: D = 3.2 mm

2.3 Width b of the Metal-Plate Waveguide

In order to have precise dimensions for the hollow-plate waveguide, support plates (either metal or glass) are placed on both sides of the waveguide, as shown in Figure 3. Hence, the hollow-plate waveguide can be considered as a section of a hollow rectangular straight waveguide. Its loss coefficient in transmitting the TE modes can be expressed as:[4]

$$\alpha_{TE} = \frac{\lambda^2}{a^3} \mathrm{Re}(1/\nu) + \frac{\lambda^2}{b^3} \mathrm{Re}(\nu) \qquad (6)$$

Therefore, when the waveguide height a and index of refraction v of the material are fixed, the wider b is the smaller the loss is. For a hollow rectangular copper waveguide, choose a = 3 mm, b = 10 mm, v = 14.2-[?] 16.4, then one can derive α = 0.0016. Transmission efficiency per meter is greater than 99 percent. Therefore, it is reasonable to choose b to be greater than 10 mm.

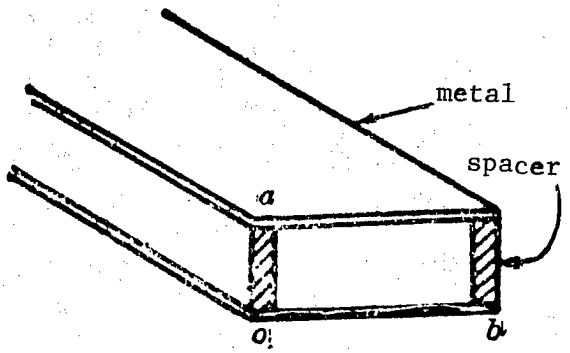

Figure 3. Simplified Schematic of Flat-Plate Waveguide Structure

III. Experimental Results

Based on the above theoretical design, we constructed two lasers. Their structural parameters and experimental results are shown in Table 1. In addition to being highly polarized, the power output level of these two lasers is comparable to the highest level achieved by other lasers of similar size built in China. This indicates that the design is successful. Furthermore, the power output and stability were found to be better than lasers without metal-plate waveguides. This is probably due to the fact that the metal plate reduced the distance between the cavity mirror and the waveguide entrance, thus lowering its loss.

Table 1. Laser Structural Parameters and Experimental Results

No.	Laser Length (mm)	Discharge Tube Diameter (mm)	Plate Waveguide Length (mm)	Plate Waveguide Width (mm)	Plate Waveguide Height (mm)	Power Output (w)	Degree of Polarization
I#	330	3.2	30	10	3	7.5	>98%
II#	470	3.5	35	10	3.2	9.0	>98%

The authors wish to express their gratitude to Professor Feng Zhichao [7458 1807 6389] for his assistance in writing this paper, and to Zheng Huaqin [6774 5478 3830], Hong Yonghe [3163 3057 0735], and Zhang Xiaojun [1728 0879 6511] for their assistance in fabricating the laser tubes.

References

1. Wang Ruifeng, et al., ZHONGGUO JIGUANG [CHINESE JOURNAL OF LASERS], Vol 14(4), p 210 (1987).

2. R. L. Abrams, IEEE J. QUANT. ELECTR., Vol QE-8, p 838 (1972).

3. E. A. J. Mareatili and R. A. Schmelzer, BELL TECH J., Vol 43, p 783 (1964).

4. M. Garmire, et al., IEEE J. QUANT. ELECTR., Vol QE 16(1), p 23 (1980).

5. Qinghua University and Chengdu Institute of Radio Engineering, "Principles of Lasers," National Defense Publishing House, 1980, p 399.

Development of New Gallium Arsenide Devices Reported

1.55-Micron GaInAsP DFB-DC-PBH Laser Diode

90CF0240a Beijing BANDAOTI XUEBAO [CHINESE JOURNAL OF SEMICONDUCTORS] in Chinese Vol 10 No 9, Sep 89 pp 712-716 [MS received 31 Aug 88]

[Article by Zhao Songshan [6392 1529 1472], Ma Pan [7456 4323], Zhou Ning [0719 1337], Yang Xinmin [2799 2450 2404] and Dong Zhijiang [5516 1807 3068] of Telecommunications Devices Corporation of Wuhan Institute of Posts and Telecommunications: "1.55 μm GaInAsP/InP DFB-DC-PBH Laser Diode"]

[Text] **Abstract**

Low-temperature liquid phase epitaxy was performed on the n-InP substrate or GaInAsP waveguide layer after a second-order grating was engraved by holographic lithography with an argon-ion laser. Afterward, a DFB-DC-PBH LD (distributed feedback double-channel planar buried heterostructure laser diode) was made using existing techniques for fabricating DC-PBH laser diodes. At 15°C, the lowest CW (continuous wave) threshold current is 63 mA and the typical value is 70~120 mA. The linear optical output power is greater than 4 mW. Its external differential quantum efficiency is 5~8.3 percent. The temperature coefficient of the primary mode wavelength λ_0, $\Delta\lambda/\Delta T$, is 0.8~1.0 Å/°C. It operated better in its static single longitudinal mode; at 400 Mbits/s, 700 Mbits/s and 1.4 Gbits/s, under 20 mA pulse current [pseudo] random code modulation, the single longitudinal mode remained in good stability. Under similar conditions, the DC-PBH LD single longitudinal mode became multiple modes or jumped mode.

Key words: Distributed feedback, second-order grating, low-temperature liquid phase epitaxy, high-bit-rate modulation, dynamic characteristics.

1. Introduction

A distributed feedback laser diode (DFB-LD) uses a grating for mode selection.[1,2] The unique feature is that it remains stable in single-mode operation with high-bit-rate modulation. Therefore, it is an ideal light source for high-capacity, long-range fiber-optic communications and coherent optical communications.

II. Structure and Fabrication

The typical structure of a distributed feedback double-channel planar buried heterostructure laser diode (DFB-DC-PBH) is shown in Figure 1. Three layers are grown on the N-InP substrate by liquid phase epitaxy: an N-InP buffer layer ($N = 2 \times 10^{18}cm^{-3}$, $d = 5$ μm), a 1.55-μm wavelength GaInAsP active layer ($d \sim 0.15$ μm), and a 1.3-μm wavelength P-GaInAsP waveguide layer ($P \approx 2\sim5 \times 10^{17}$, $d \sim 0.2$ μm). The second-order grating was engraved by holographic lithography using a Mach-Zehnder optical path; a domestic argon-ion laser (wavelength 4579 Å) manufactured by the Nanjing Electron Tube Factory was employed. The grating was etched chemically to form sinusoidal or near-rectangular grooves that are 4600 Å apart and 800~1200 Å deep. A layer of P-InP ($P = 3\sim8 \times 10^{17}cm^{-3}$, $d = 1\sim2$ μm) was then grown on the grating using low-temperature liquid phase supercooled epitaxy. Finally, the existing DC-PBH laser fabricating technique[3,4] was used to prepare the DFB-DC-PBH laser diode.

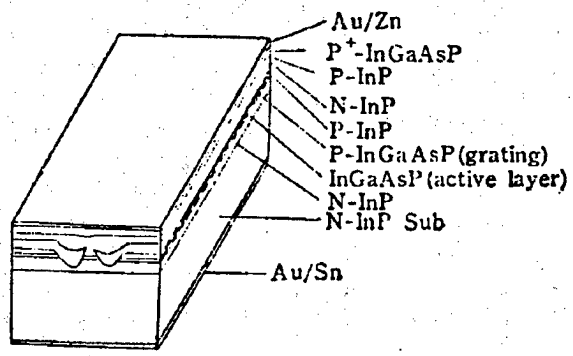

Figure 1. The DFB-DC-PBH LD Structure

III. Performance Characteristics

1. Dependence of Optical Power Output Upon Injection Current

The dependence of the device's optical output power P upon injection current I as a function of temperature was measured, as shown in Figure 5. The threshold current of that device is 63 mA (at 15°C) and the optical output power is approximately 2 mW at 25°C. Most of the devices have a threshold current of 70~130 mA, a linear optical power of over 4 mW, normal optical power of 6~7 mW, and an external differential quantum efficiency of 5~8.3 percent.

2. Spectra

A Japanese-made Model 1425 spectrometer and an American-made thermostatic bath were used to measure the output spectra of all the DFB laser diodes at 0.5~2 mW. Single-longitudinal-mode lasers were selected based on current standards adopted in China wherein a single longitudinal mode has a primary to secondary mode-suppression ratio of more than 10 dB. Then, the suppression ratio, the spectral half width, the temperature drift coefficient $\Delta\lambda/\Delta T$ of the primary-mode wavelength λ_0, and the dynamic spectra were determined in detail.

(1) **Effect of Cavity Length on Mode**

The cleavage cavity length L is 130, 200, or 320 μm. Approximately 15~30 percent of them are single-longitudinal-mode laser diodes. The longer the cavity is, the more single-longitudinal-mode devices there are and the better the suppression ratio becomes. This illustrates the mode selection function of the grating.

(2) **Primary to Secondary Mode-Suppression Ratio and Spectral Half Width**

First, the effect of the spectrometer on suppression ratio and spectral half width was observed in order to obtain more accurate data. A large number of spectra obtained showed that the slit width of the spectrometer has no apparent effect on the suppression ratio. However, it has a significant effect on the half width of the spectrum. The slit width of the Japanese-made 1425 spectrometer is expressed in terms of resolution R_{es}. Once R_{es} is manually set, the instrument automatically adjusts its slit width. The minimum resolution of the instrument is R_{es} = 0.1 nm. We used three settings, i.e., R_{es} = 0.1, 0.2 and 0.5 nm, in our experiments. The suppression ratio of the laser diode DFB23# essentially remained at around 18 dB (curves omitted), while the spectral half widths of the primary mode are 0.1, 0.2 and 0.4 nm, respectively, as shown in Figure 2.

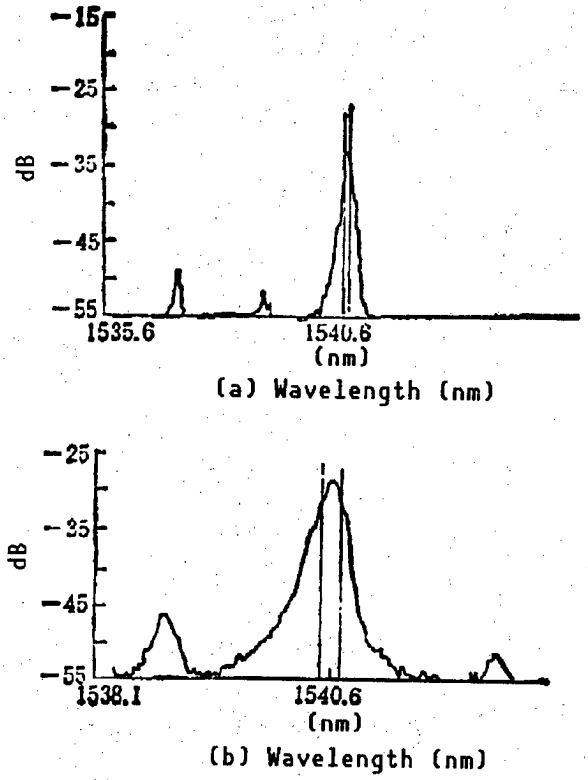

Figure 2. Spectrometer Slit Width (R_{es}) Vs. Spectral Half Width of Laser Primary Mode
(a) R_{es} = 0.1 nm; (b) R_{es} = 0.2 nm

Considering the fact that the minimum resolution of the spectrometer is 0.1 nm, the half width of the primary mode spectrum of 27#DFB-LD should be less than 1.4 Å. Therefore, in order to obtain more accurate data, we must use a higher-resolution spectrometer or monochromator. In conclusion, after taking the fact that the DFB spectral half width is small into account, we basically chose R_{es} = 0.1 nm to measure various parameters in this work. The single-longitudinal-mode suppression ratios thus measured are 10~18 dB. Most of the primary-mode spectral half widths are less than 1.4 Å, while a few of them are around 2 Å (because it is either 0.1 nm or 0.2 nm from the recorded curve).

(3) Temperature Drift Coefficient $\Delta\lambda/\Delta T$ of Primary Mode Wavelength λ_0

The temperature drift coefficient $\Delta\lambda/\Delta T$ of the primary-mode wavelength λ_0 is an important parameter differentiating a DFB laser from a conventional F-P [Fabry-Perot] cavity laser. The domestic standard is $\Delta\lambda/\Delta T \leq 1.5$ Å/°C, while the international reported value is about 1 Å/°C and for a conventional F-P cavity laser $\Delta\lambda/\Delta T$ is 3~5 Å/°C. We tested over a dozen single-longitudinal-mode laser diodes and found that $1.2 \text{ Å/°C} \geq \Delta\lambda/\Delta T \geq 0.7$ Å/°C. Most of them are between 0.8~1.0 Å/°C. Figure 3 shows the curves for primary-mode wavelength λ_0 versus temperature T for DFB-LD 29# and 54#. For the 29# DFB-LD, $\Delta\lambda/\Delta T$ = 1.0 Å/°C when the optical output power is fixed at 0.5 mW, and $\Delta\lambda/\Delta T$ = 0.91 Å/°C when the optical output power is fixed at 1.4 mW; for the 54# DFB-LD, $\Delta\lambda/\Delta T$ = 0.86 Å/°C when the optical output power is maintained at 1.5 mW or 2 mW. Using the same technique, the $\Delta\lambda/\Delta T$ of a single-longitudinal-mode 1.3-μm DC-PBH LD is 3.7~4.0 Å/°C. These results are consistent with the data reported for similar devices elsewhere in the world.

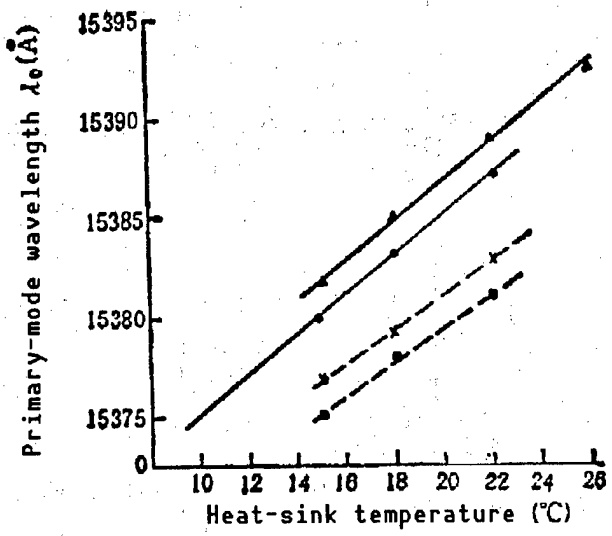

Figure 3. DFB-LD Primary-Mode Wavelength λ_0 Vs. Heat-Sink Temperature

20# DFB-LD
●: P = 0.5 mW
▲: P = 1.4 mW

54# DFB-LD
□: P = 1.5 mW
x: P = 2.0 mW

(4) Dynamic Modulation Spectrum

When a conventional F-P cavity laser operates at a high rate, the single longitudinal mode either becomes multiple modes or jumps into another mode. Thus, it limits communications capacity and transmission range. The DFB laser, however, can remain in single-longitudinal-mode operation. Hence, a high-rate modulation spectrum, i.e., a dynamic modulation spectrum, is an important standard that differentiates a dynamic single-longitudinal-mode laser from a conventional F-P cavity laser. It is also the foundation for use in high-rate communications systems. Figure 4 shows a block diagram that describes the apparatus used to measure dynamic spectra.

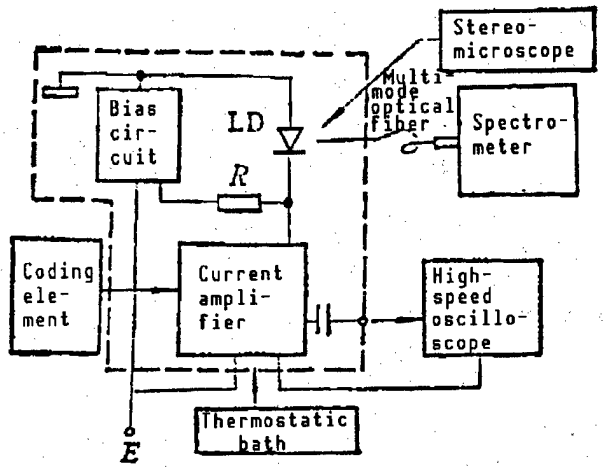

Figure 4. Experimental Apparatus for Measuring Dynamic Spectra of DFB-DC-PBH LD

The code element shown in the figure is an imported Model ME522A Transmitter, 0~700 Mbits/s. It can reach 1.4 Gbits/s if return-to-zero [RZ] coding is employed. The bias circuit for the DFB-LD, the current amplifier, the laser device, and the wireless capacitor C_f were also soldered on a circuit board and maintained at a constant temperature. The Model 7904 high-speed oscilloscope, with a 14-GHz bandwidth, is used to monitor the pulse waveform applied on the DFB-LD through C_f. A high-speed PIN detector with a fiber pigtail was also used to observe the pulse applied to the DFB-LD and pulse waveform generated. (Many pictures have been taken already.) The spectrometer is an ANDO Model AQ-1425, which uses a Ge-APD [germanium avalanche photodiode] detector. It also includes a computer memory sampling system, a CRT display and a printer to facilitate the experimentation.

Figure 5 shows the dependence of optical output power upon injection current at different temperatures. It also shows the spectra at different optical output power levels (i.e., various values of bias current I_b) when the 20-mA pulse current (I_p) is randomly modulated at 700 Mbits/s. The stability of the single longitudinal mode is apparent.

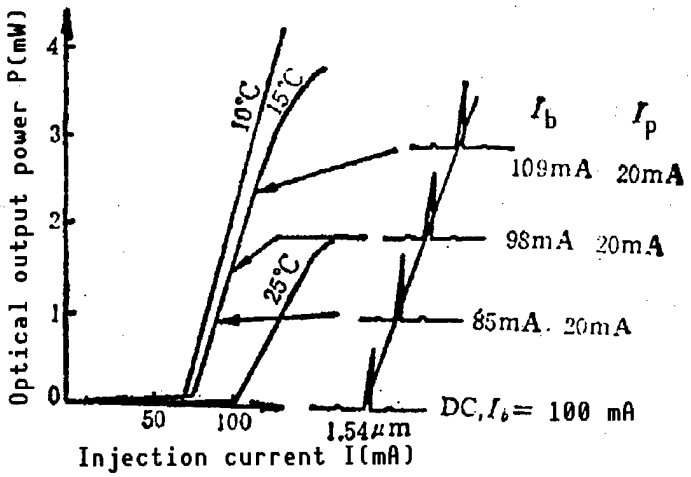

Figure 5. P-I Curve for DFB-DC-PBH LD and Its 700 Mbps Modulation Spectra

Figure 6 shows the spectral characteristics at various modulation rates. These are DFB-LD spectra measured at a fixed bias current I_b (corresponding to 2 mW optical output power), with a 20-mA pulse current random-code modulated at 400 Mbits/s, 700 Mbits/s and 1.4 Gbits/s, respectively.

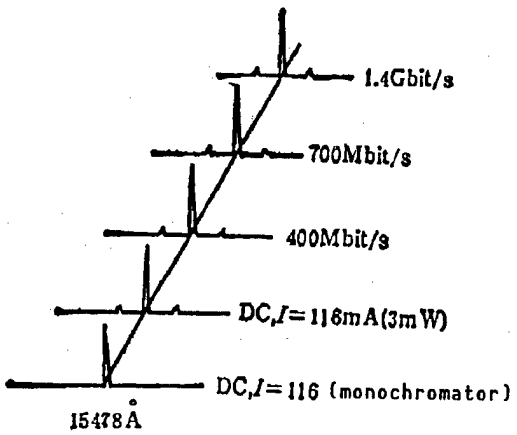

Figure 6. Stable Single-Longitudinal-Mode Operation of a DFB-DC-PBH-LD at Various Modulation Rates
(400 Mbits/s, 700 Mbits/s, 1.4 Gbits/s; pulse current 20 mA)

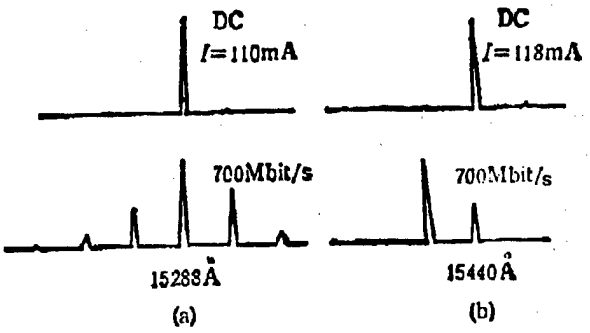

Figure 7. DC-PBH LD High-Rate Modulation Spectra
(a) 700 Mbits/s, 200-mA pulse current—Single longitudinal mode becomes multiple modes
(b) 700 Mbits/s, 20-mA pulse current—Single longitudinal mode jumps mode

Figure 7 shows the modulation spectra for a conventional F-P cavity DC-PBH laser. At an identical modulation rate, after repeated testing, the single longitudinal mode of the DC-PBH laser either became multiple modes or jumped mode without exception. The dynamic spectrum of a DFB-DC-PBH laser diode,

however, remains relatively stable as long as it has good single-longitudinal-mode characteristics.

IV. Discussion

Because the DFB-LD grating does not have a $\lambda/4$ phase shift and was not treated at the ends, only 5~30 percent of the devices are single-longitudinal-mode devices and the suppression ratio is not high enough (compared to early-stage devices reported abroad). Research on a $\lambda/4$-phase-shift grating should be accelerated to increase the yield of single-mode devices. The performance of the device reflects our preliminary success. Factors such as grating shape, groove depth and epitaxy technique still need to be improved and enhanced. In our experiment, because of the use of a fiber coupler and converter (at the junction of the fiber and the spectrometer), the suppression ratio obtained from the static spectrum is slightly different from that measured with a monochromator. This is yet to be resolved.

The authors wish to thank Wang Suqin [3769 4790 3830] for assembling the laser diodes, Sun Zhenxing [1327 2182 5281] of the Institute of Optical Communications in the Research Institute of Posts and Telecommunications Science, and Wang Zhiguang [3769 0037 0342] at the test facility for their support.

References

1. Haruo Nagai, et al., IEEE, QE-22, 450 (1986).

2. H. Kogolnik and C.V. Shonk, J. APPL. PHYS., 43, 2327 (1972).

3. Zhao Songshan, et al., BANDAOTI XUEBAO [CHINESE JOURNAL OF SEMICONDUCTORS], 7, 324 (1986).

4. Ibid., Proceedings of the National Academic Conference on Optical Communications Devices, Changchun, pp 17-24 (1985).

GaAs/AlGaAs MQW Laser Diode

90CF0240b Beijing BANDAOTI XUEBAO [CHINESE JOURNAL OF SEMICONDUCTORS] in Chinese Vol 10 No 10, Oct 89 pp 788-793 [MS Received 19 Aug 88]

[Article by Zhang Yonghang [1728 3057 5300], Kong Meiying [1313 2734 1758], Chen Lianghui [7115 5328 1920] and Wang Qiming [3769 0796 2494] of the Institute of Semiconductors, Chinese Academy of Sciences, Beijing: "GaAs/AlGaAs Multiple Quantum Well Laser," a National Natural Science Foundation-funded project]

[Text] **Abstract**

Multiple quantum well (MQW) laser structures were made using a domestically developed molecular beam epitaxy system. At room temperature, the broad-contact-area threshold current density for the devices is 3000 A/cm^2. The

optimal threshold current obtained for a single device with a proton-bombarded stripe geometry is 128 mA. The single-face continuous power output is over 22 mW. This device can operate in a single longitudinal mode within a certain injection range. The maximum single-face differential quantum efficiency is 34 percent and the lasing wavelength is 8590-8640 Å. The far-field light-intensity distribution shows a single peak. Near room temperature, its characteristic temperature T_c is 202 K. Preliminary studies on the epitaxial materials and devices show that the quality of AlGaAs, especially doped AlGaAs, is not ideal, which might be the reason why the threshold current density of the laser is insufficiently low.

Key words: molecular beam epitaxy, quantum well, semiconductor laser.

I. Introduction

Since the superlattice was introduced by Esaki and Zhu Zhaoxiang [2612 6392 4382],[1] and as super-thin-layer epitaxial techniques have been developed and perfected, multiple quantum well (MQW) and single quantum well (SQW) lasers of various structures have been fabricated.[2] A quantum-well laser with real practical use potential was first successfully made by W.T. Tsang[3] in 1979 using MBE [molecular beam epitaxy]. Since then, a number of scientists have successfully fabricated high-level quantum-well lasers using techniques such as MBE, MOCVD, etc. Compared to the double-heterojunction lasers in the past, these new ones have a variety of advantages such as low threshold current density, variable lasing wavelength dependent upon well width, high TE and TM mode-gain differential, better high-frequency modulation characteristics, a threshold current less affected by temperature, etc. This is a new generation of semiconductor laser with a great deal of potential.

Through continuous analysis of epitaxial materials to improve and optimize various epitaxial processes such as control of growth rate, dopant concentration and composition, usable MQW epitaxial wafers were grown in a domestically developed MBE device. As a result of further fabrication, MQW lasers that can operate continuously at room temperature have been obtained. The relevant characteristics and physical analysis of these lasers are also given in this paper.

II. Device Fabrication

The MQW structures were grown with a Chinese-made MBE device[4] which consists of a growth chamber and a sample-entry chamber. The growth chamber has six source furnaces and some real-time detection equipment such as a high-energy electron diffractometer (HEED), a quadruple mass spectrometer, and an ultrahigh-vacuum gauge. These devices are used for surface analysis, growth-process monitoring, and residual-gas analysis and vacuum measurement, respectively.

The structure grown is shown in Figure 1. Typically, the parameters are a 1.5-micron Si-doped ($n = 1 \times 10^{18}cm^{-3}$) GaAs buffer layer; a 1.5-micron Si-doped ($N = 5 \times 10^{17}cm^{-3}$) $Al_xGa_{1-x}As$ light-restriction layer ($x = 0.24$); an undoped active layer, which consists of 10 wells, each having a well width of 100 Å,

a barrier width of 50 Å, and a potential-barrier composition of $Al_yGa_{1-y}As$ (y = 0.16); and a 1.5-micron Be-doped (P = 5 x $10^{17}cm^{-3}$) $Al_xGa_{1-x}As$ light-restriction layer; and a 1.5-micron Be-doped (1 x $10^{18}cm^{-3}$) GaAs top layer to facilitate the making of an ohmic-contact electrode. In order to demonstrate the advantages of quantum-well lasers, we used the same MBE system to make double-heterojunction lasers of similar layer structure. The difference is the active layer, which is a 0.16-micron-thick undoped GaAs layer.

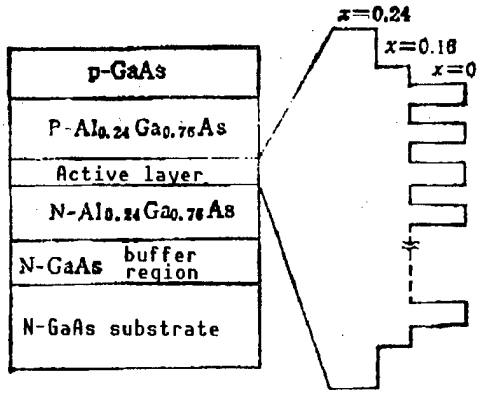

Figure 1. Structure of a MQW Laser

In material preparation, the cleaning and polishing of the GaAs substrate, the removal of adsorbed gas from the substrate and molybdenum prior to the growing process, and the selection of growth temperature are critical to obtaining high-efficiency lasing materials.

After going through steps such as In removal, Zn diffusion, electrode evaporation and alloying, the epitaxial wafer is cleaved into broad-contact-area diodes. Those with lower threshold current were chosen to be fabricated into stripe-geometry laser diodes. In this work, we mainly used proton-bombardment stripes and oxide stripes. The depth of proton bombardment is 2 microns. The masking tungsten wire diameter is 8~10 microns and the cavity of the device is approximately 150~200 microns in length.

III. Characteristics of the Quantum Well Laser Diodes

The threshold current density of a typical MQW laser is around 4000 A/cm^2 and may get as low as 3000 A/cm^2. Figure 2 shows the curve for single-face light power output versus injection current. It was obtained under continuous injection at 28.5°C (on sample B67-7).

Figure 3(a) and (b) shows how emission spectra vary with current for dc operation of an MQW laser and a DH laser, respectively. A comparison shows that the lasing wavelength of the MQW laser has already shifted toward a shorter wavelength relative to that of the DH device, and the quantum effect is apparent. The amount of shift agrees with theoretical calculation. The figure also indicates that the MQW laser can operate in a single longitudinal mode within a certain current range. Figure 4(a) and (b) shows the far-field patterns of the MQW laser perpendicular and parallel to the junction plane under dc, respectively. The fact that there is only a single peak suggests

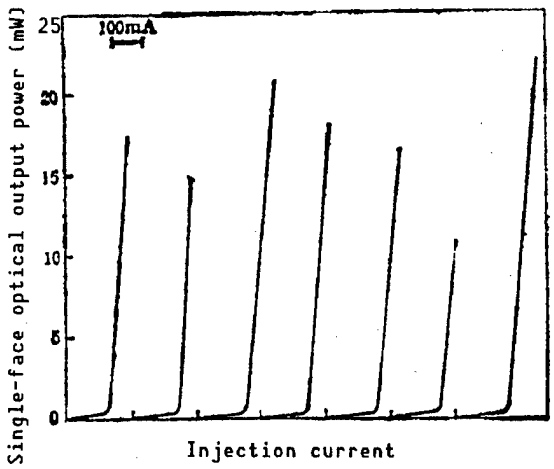

Figure 2. MQW Laser Power Output Vs. Injection Current

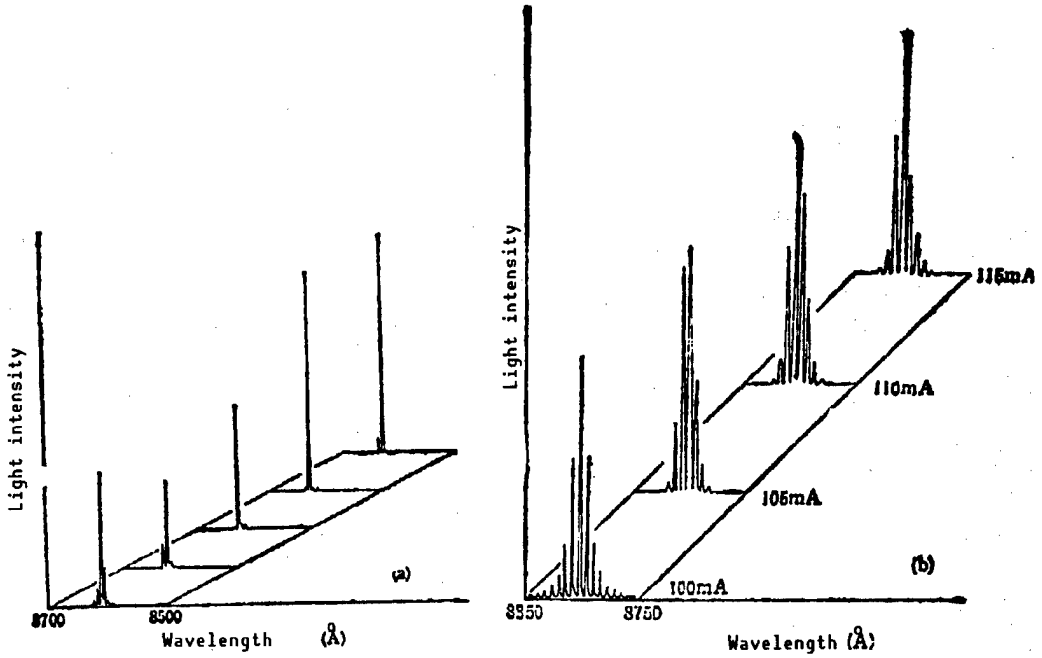

Figure 3. Spectra for MQW LD and DH LD at Various Injection Currents
(a) MQW, continuous, 28.5°C; (b) DH

the device operates in its basic transverse mode. From the typical device parameters shown in Table 1, it is apparent that some devices have a higher external differential quantum efficiency and very close lasing wavelengths. This indicates that the active region of the device, i.e., the epitaxially grown MQW materials, is uniform.

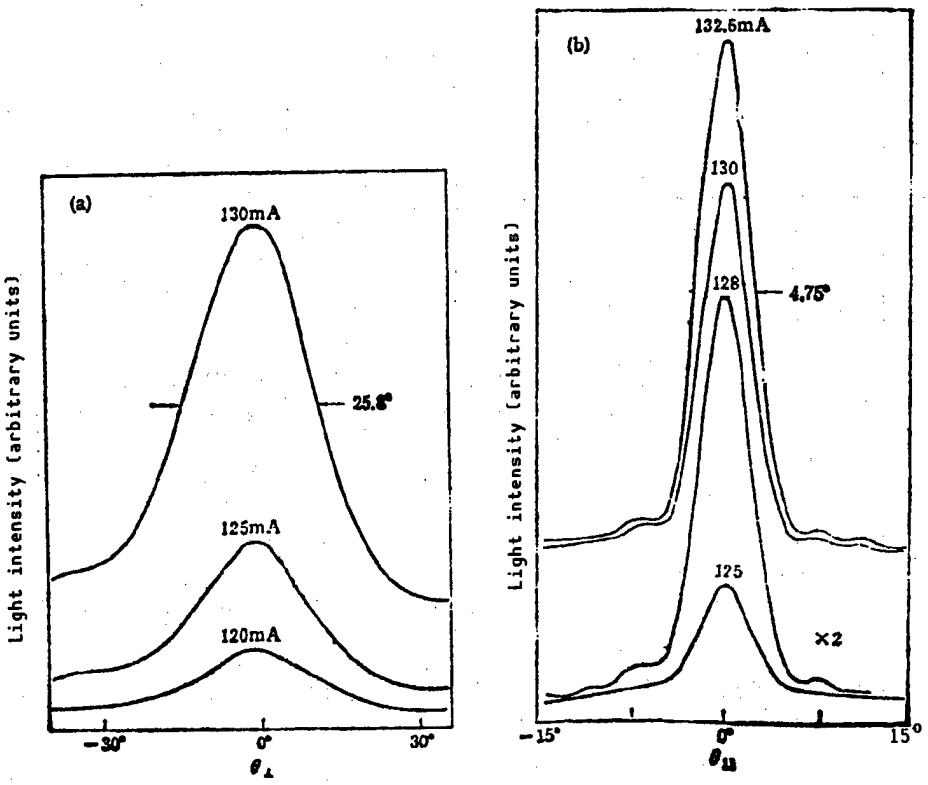

Figure 4. Far-Field Pattern of MQW Laser Diode (B67.1, room temperature)
(a) Perpendicular to junction plane;
(b) Parallel to junction plane

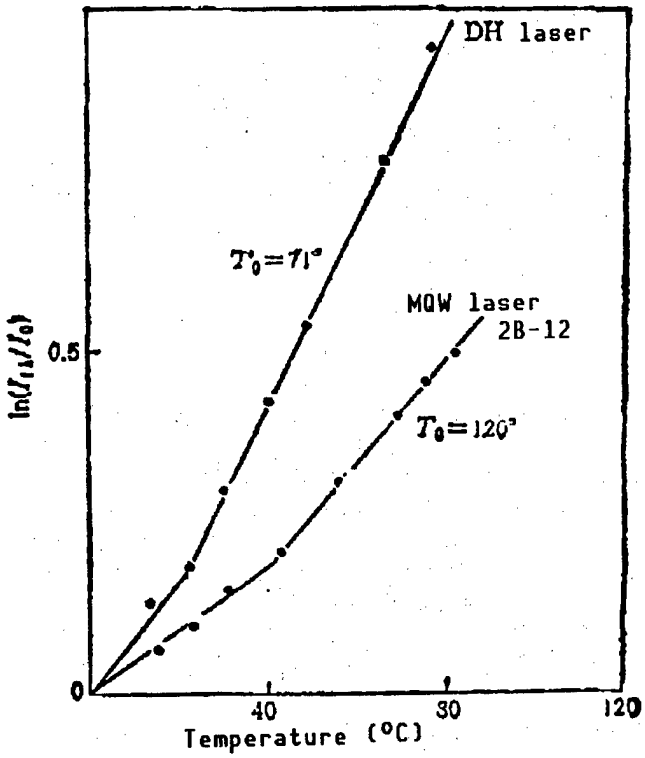

Figure 5. Threshold Current Vs. Temperature for an MQW Laser

Table 1. Typical Parameters for Several MQW Lasers

No.	Threshold current (mA)	External differential quantum efficiency (%)	Series resistance (Ω)	Forward on-state voltage (V)	Reverse breakdown voltage (V)	Center lasing wavelength (Å)
B67-1	128	19	–	–	–	8593
-4	130	–	–	–	–	8610
-6	155	34	3	~1.2	8.0	8627
-7	164	19	–	–	–	8628
-11	178	22	2	~1.2	6.8	–
-12	154	30	3	~1.2	3.5	8611
-13	158	22	3	~1.2	–	–
-14	178	24	–	~1.2	–	8623
-15	160	29	4	~1.2	7.0	–
-16	128	23	2	~1.2	7.0	8633
-17	178	20	2.5	~1.2	6.0	–
-19	165	19	3	~1.2	6.0	–

Figure 5 shows the dependence of MQW laser threshold current upon temperature. This relation can be expressed empirically as:

$$I_{th}(T) = I_0 \cdot \exp\ (T/T_0)$$

where I_0 is the threshold current at 0°C. An MQW laser compared to a DH laser may have a higher T_0, as high as 202 K.

IV. Results and Discussion

For a quantum-well laser, we must admit that the threshold current density obtained in this work is high. To this end, we made the following analysis.

Scanning electron micrographs of the laser structures and HEED patterns obtained in the growing process showed that the interface between the N-$Al_{0.23}Ga_{0.77}As$ light-restriction layer and the n-GaAs buffer layer is smooth and the interface between the N-$Al_{0.23}Ga_{0.77}As$ layer and the active layer is bumpy.

Photoluminescence spectra of a sample undoped $Al_xGa_{1-x}As$ light-restriction layer and a sample Si-doped $Al_xGa_{1-x}As$ light-restriction layer showed that the undoped layer sample has obvious MQW luminescent characteristics. Emission peaks corresponding to electron transitions to heavy holes and light holes can be clearly identified. The spectrum of the silicon-doped specimen, however, is very wide and the quantum efficiency is very poor. This demonstrates that the quality of the necessary Si-doped AlGaAs restriction layer has a great-effect on the light-emitting characteristics of the MQW laser.

The photoluminescence spectrum was measured with the top P-GaAs layer selectively etched out. It was found that light emitted from the P-AlGaAs

layer of a high-threshold current density epitaxial wafer is weaker in intensity compared to that from a high-quality AlGaAs material. The MQW fluorescence is even weaker. This indicates the presence of a high concentration of nonradiation recombination centers in the P-AlGaAs layer. There are too few light-producing carriers falling into the well after diffusion. We also noticed that the half-height width of the MQW emission peak is wider, which suggests that the quality of the MQW itself needs to be improved. It is also seriously impacted by the upper restriction layer which makes its threshold current density intrinsically high.

In addition, deep-level transient spectroscopic (DLTS) analysis of some MQW laser devices showed a high-concentration ($1.8 \times 10^{17} cm^{-3}$) deep energy-level center in the N-AlGaAs restriction layer.

In conclusion, the high threshold current density of the MQW lasers is mainly due to the insufficiently high quality of the AlGaAs materials, particularly the Si-doped AlGaAs materials. In addition, the bumpiness of the interface also adversely affects the threshold current density.

V. Conclusions

We have successfully fabricated room-temperature continuously-lasing MQW lasers using a domestically developed MBE system. The optimal threshold current is 128 mA and the maximum single-face continuous power output is 22 mW. The lasing wavelength range is 8590~8640 Å. The single-face external differential quantum efficiency is as high as 34 percent and the characteristic temperature is 202 K.

An analysis of the materials and device characteristics showed that the threshold current of the MQW laser is insufficiently low because the quality of the AlGaAs materials, especially the doped AlGaAs materials, is not ideal. Further improvements are in progress.

The authors wish to thank Xu Junying [1776 0193 5391], Li Likang [2621 4539 1660], Zeng Yiping [2582 0001 1627], Liang Jiben [2733 1015 2609], Sun Dianzhao [1327 3013 3564], Gao Jilin [7559 1323 2651], and other people associated with the processing line in the seventh laboratory for their assistance in epitaxy, laser fabrication and measurements.

References

1. Leo Esaki, IEEE J. QUANTUM ELECTRONICS, QE-22 (9), 1611 (1986).

2. N. Holonyak, Jr., SOV. PHYS. SEMICOND., 19, 913 (1985).

3. W.T. Tsang, C. Weisbuch, R.C. Miller and Dingle, APPL. PHYS. LETT., 356, 73 (1979).

4. MBE equipment development group, BANDAOTI XUEBAO [CHINESE JOURNAL OF SEMICONDUCTORS], 2, 164 (1981).

1.5-μm InGaAsP/InP RW-DFB Laser Diode

90CF0240c Beijing BANDAOTI XUEBAO [CHINESE JOURNAL OF SEMICONDUCTORS] in Chinese Vol 10 No 10, Oct 89 pp 794-798 [MS received 24 Mar 89]

[Article by Wang Wei [3769 0962], Zhang Jingyuan [1728 7234 1254], Tian Huiliang [3944 1979 5328], Miao Yubo [4924 5148 0590], Wang Xiaojie [3076 1321 2638], Ma Chaohua [7456 2600 5478], Wang Liming [3769 7787 2494], Lü Hui [0712 0583], Gao Junhua [7559 0193 5478] and Gao Honghai [7559 3163 3189] of the Institute of Semiconductors, Chinese Academy of Sciences: "1.5 μm InGaAsP/InP RW-DFB Laser"]

[Text] **Abstract**

A 1.5-μm InGaAsP/InP RW (ridge waveguide) DFB (distributed feedback) laser was fabricated by a two-step LPE (liquid phase epitaxy) process. Its dc optical output power exceeds 6 mW at room temperature without any kink, its threshold current is 34 mA, and its single-face external differential quantum efficiency is as high as 33 percent. It operates in a single longitudinal mode over a 43°C range [2°C to 45°C] around room temperature. The wavelength temperature coefficient is 0.9 Å/K. The static [spectral] line width is 60 MHz at 1.6 mW output power. The output remains in a single longitudinal mode under 1-GHz sinusoidal modulation.

Key words: Ridge waveguide, distributed feedback laser, dynamic single laser.

I. Introduction

As far as using 1.55-μm single-mode optical fiber for high-capacity, long-range optical communications is concerned, its transmission bandwidth is seriously limited by the dynamic spreading of the emission spectrum of the source.[1] In order to overcome this problem, a periodic diffraction grating was developed to replace the cavity-surface feedback in common lasers so that light is only amplified at the wavelength determined by the grating cycle; this was based on the coupled-wave theory introduced by H. Kogelnik.[2] Thus, it has mode-selection capability. In the early 1980's, 1.5-μm GaInAsP/InP DFB[3] and DBR [distributed Bragg reflector][4] lasers that can remain in a single longitudinal mode under high-rate modulation have been developed.

Currently, researchers are exploring techniques to improve the characteristics of grating lasers for use in coherent optical communications and integrated optical circuitry in the future. As an example, Y. Suematsu recently introduced a DR laser.[5] People are taking steps to develop this type of laser to meet market demand. To this end, it is necessary to simplify its structure and technique to make it manufacturable. For example, Thomson Laboratories in France has introduced a buried-waveguide structure[6,7] and West Germany is developing a mass-transport version of the DFB laser.[8]

The 1.5-μm RW-structure DFB laser is also the result of an attempt to raise modulation rate and to simplify the fabrication technique.

II. Structure and Preparation

In order to reduce capacitance to raise the modulation rate and to simplify the fabrication process to improve yield, the ridge waveguide structure was chosen.[9] Figure 1 shows a schematic diagram of this structure. First, a conventional LPE technique was used to prepare a 1.5-μm InGaAsP/InP laser.[10] An n-InP transition layer (Te-doped, 5 x $10^{18}cm^{-3}$, 6~8 μm thick), an undoped active layer (λg = 1.5 μm, 0.15 μm thick), and a P-InGaAsP waveguide layer (λg = 1.3 μm, Zn-doped, 2~3 x $10^{17}cm^{-3}$, 0.2 μm thick) are grown on an n-InP substrate. Then an optical grating, approximately 800~1000 Å deep with a cycle [spacing] of 2300 Å or 4600 Å is engraved on the InGaAsP waveguide layer with holographic lithography.[11] The cycle Λ for each experiment must be determined by the formula $\Lambda = m\lambda_p/2n_e$, where λ_p is the transmission wavelength; its value can be determined from the photoluminescent peak of the original epitaxial wafer. The variable n_e is the effective index of refraction in the grating waveguide region; it is derived numerically from a five-layer planar waveguide model.[12] After engraving the grating on the original epitaxial wafer, it is used as a substrate to grow a P-InP restriction layer (Zn-doped, 5 x $10^{17}cm^{-3}$, 1.5 μm thick) and a P-InGaAsP top layer (Zn-doped, $10^{18}cm^{-3}$, 0.3 μm thick) by LPE at 590°C. The ridge waveguide structure shown in Figure 1 is then selectively etched along the <110> direction using conventional photolithography and reactive ion etching (RIE); each RW strip is approximately 4 μm wide. Figure 2 [not reproduced] is a micrograph of the top view of the ridge. The surface of the second-order grating after completion of the two-step epitaxial process was clearly exposed by selective etching with $HCl:H_2O$ = 4:1. It shows that the interface between the waveguide layer and the InP restriction layer goes up and down periodically after the two-step LPE process and the period is determined by the grating. Finally, a high-performance aluminum-oxide insulation film and electrode windows with less than 5-ohm series resistance are obtained by high-frequency sputtering and conventional electrode-making technique. The diode is typically 300 μm (width) x 200 μm (length).

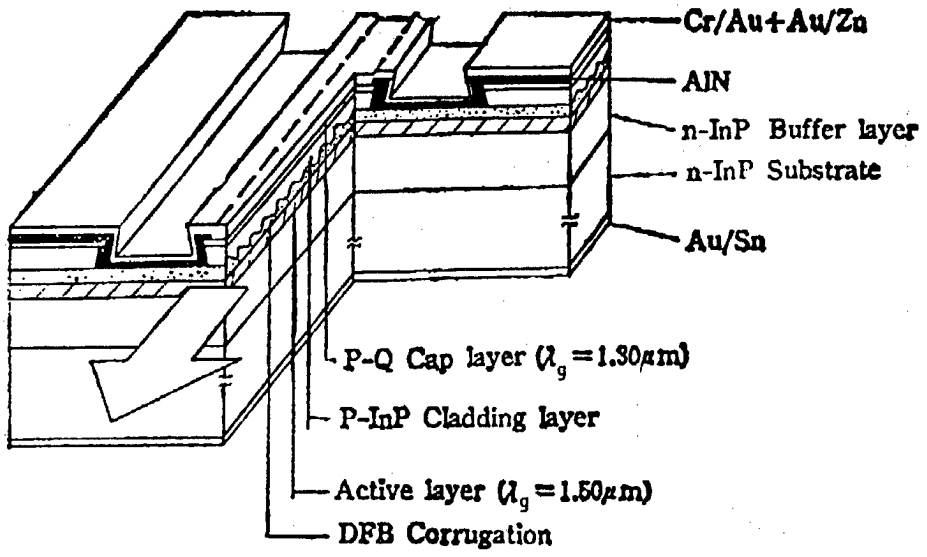

Figure 1. Structure of the RW-DFB Laser

III. Characteristics and Discussion

Figure 3 shows the light intensity versus current curve of a 1.5-μm RW DFB laser at room temperature (15°C) and the single-longitudinal-mode spectra at various dc driving currents. At 1.4 times threshold current, the primary-to-side-mode ratio (SMSR) is greater than 24 dB. With increasing driving current, SMSR tends to get larger; at 2.2 times threshold value, it is over 29 dB. The threshold current of the device is 34 mA at room temperature. This is the lowest threshold value obtained; typically, the room-temperature threshold is 40 mA. The highest single-face differential quantum efficiency obtained is 33 percent; usually, it is 20-25 percent. Figure 4 shows the single-longitudinal-mode spectra of a typical device at different temperatures under constant power of 1 mW. The figure shows that stable single-mode operation can be maintained over a 43°C temperature range.

The temperature coefficient of wavelength, $\Delta\lambda/\Delta T$, is 0.1 nm/deg. Figure 5 shows the L/I curves of another typical device at different temperatures. Based on the figure, the maximum lasing temperature of the device is 60°C. It also shows usually there are no kinks up to 6 mW light output power. It was experimentally discovered that kinking is often associated with mode jumping. We employed a fiber-optic ring cavity technique[13] to measure the static line width of the laser. Figure 6 [not reproduced] shows the spectrum of an RW-DFB laser at 1.6 mW output power driven at 48 mA dc (1.2 times threshold value) and observed through an 0.6-m-long optical-fiber ring cavity resonator. The free spectrum zone of the ring cavity is known to be 340 MHz. Thus, the spectral line width of this laser at 1.6 mW output is 60 MHz. It was found experimentally that with increasing light power, the line width tends to become narrower.

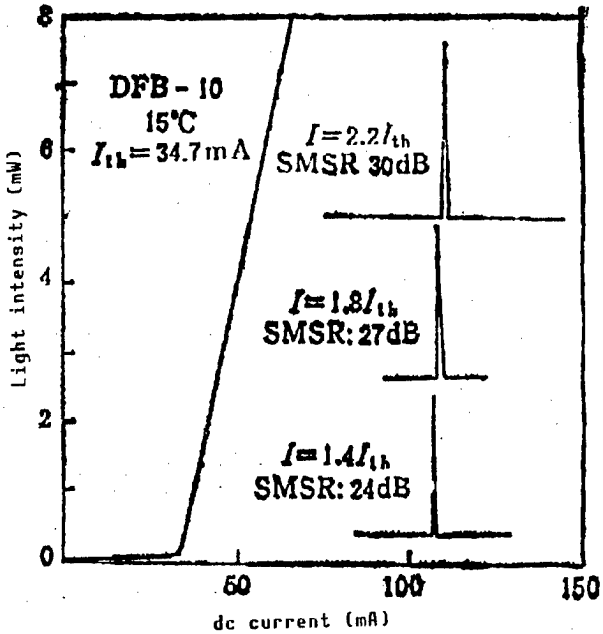

Figure 3. Light Intensity of an RW-DFB Laser Vs. Current at Room Temperature and Single-Longitudinal-Mode Spectra at Different Driving Currents

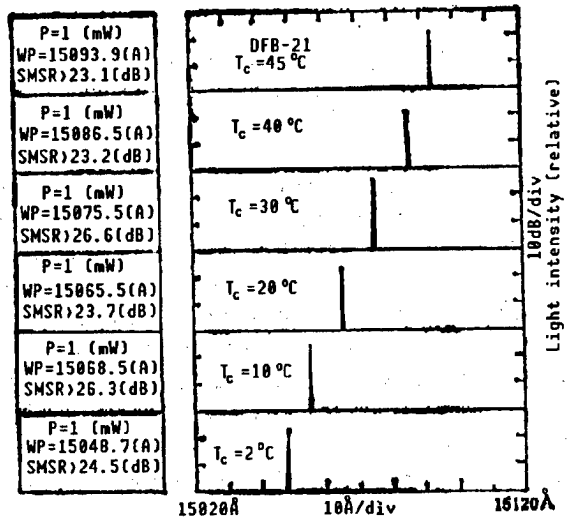

Figure 4. Single-Longitudinal-Mode Spectra of an RW-DFB Laser at Different Ambient Temperatures

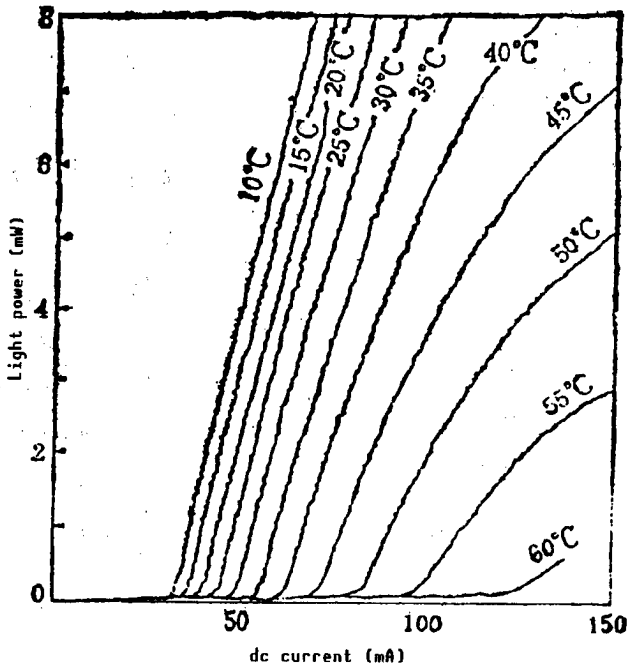

Figure 5. Highest Lasing Temperature of an RW-DFB Laser

In addition to measuring the device's static characteristics, we also measured its dynamic spectrum under 1-GHz sinusoidal modulation using an infrared scanning interferometer with a 30-GHz free-spectrum zone. Figure 7 [not reproduced] shows the dynamic spectrum obtained when the dc bias current impressed on the device was 39 mA (1.1 times threshold value), sinusoidal-modulation frequency was 1 GHz, and power-modulation depth was 50 percent. Figure 7 tells us that the light output remained in single longitudinal mode under 1-GHz sinusoidal modulation. Based on the fact that the free-spectrum

zone is 30 GHz, we estimated that the line width of the expanded dynamic single-mode spectrum is 3 GHz; that means the width of the dynamic expanded spectrum is 0.2 Å.

In order to directly verify the feedback capability of the grating in an RW-DFB laser, we conducted some experiments with a 1.5-micron-wavelength F-P cavity laser and an RW-DFB laser with their light-output faces coated with a transmission film (ZrO_2). Figure 8(a) and (b) show the light intensity versus current curves of these two lasers before and after they were coated with the transmission film, respectively. The results showed that the F-P laser became a light emitting diode (Figure 8(a)) after getting a transmission coating because the cavity lost a resonance face. As for the RW-DFB laser, because its feedback source is the grating instead of the cleaved cavity face, it not only remained lasing but also exhibited improvements in parameters such as quantum efficiency (Figure 8(b)).

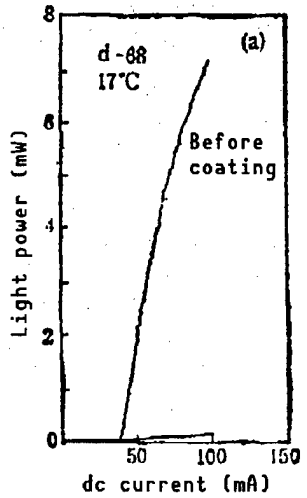

Figure 8(a). Light Intensity Vs. Current Curves of an F-P Cavity Laser Before and After Adding a Transmission Coating

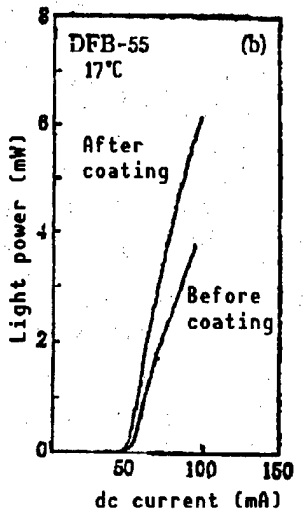

Figure 8(b). Light Intensity Vs. Current Curves of an RW-DFB Laser Before and After Adding a Transmission Coating

IV. Conclusions

Using the ridge-waveguide structure, it only takes two LPE steps to fabricate an RW-DFB laser. The room-temperature threshold current is usually around 40 mA and the lowest value is 34 mA. The device's single-face differential quantum efficiency is usually around 25 percent and has reached as high as 33 percent. It operates stably in single longitudinal mode over a 43°C temperature range near room temperature. Some devices showed kinks when their optical output power exceeded 6 mW. The static line width of the device at 1.6 mW output was measured to be 60 MHz using a ring-cavity technique. Under 1-GHz sinusoidal modulation, it remained in single-longitudinal-mode operation. The highest lasing temperature is 60°C. It is expected that the

performance of such a device can be further enhanced after ridge width is reduced and the heat-dissipation characteristic is improved.

The authors wish to thank Wu Yizun [0702 1744 1415], Zhang Hanyi [1728 3352 0001], Pan Guisheng [3382 6311 3932] and Bian Jingyi [6708 2925 5030] for their close collaboration in measuring device characteristics; Chen Jiying [7115 4764 5391] for working on RIE; and Zhang Hongqin [1728 3163 3803], Luo Liping [5012 7787 5493] and Bian Jing [6708 7234] for their support on device fabrication.

References

1. W.A. Gambling, H. Matsumura and C.M. Ragdale, ELECTRON LETT., 15, 474 (1979).

2. H. Kogelnik and C.V. Shank, J. APPL. PHYS., 43, 2327 (1972).

3. K. Utaka, S. Akiba, K. Sakai and Y. Matsushima, ELECTRON LETT., 17, 961 (1981).

4. K. Utaka, K. Kobayashi and Y. Suematsu, IEEE. J. QUANTUM ELECTRON, QE-17, 5, 651 (1981).

5. S. Pellegrino, K. Komori, H. Suzuki, K.S. Lee, S. Arai, Y. Suematsu and H. Aoki, ELECTRON LETT., 24, 7, 435 (1988).

6. A. Talneu, D. Rondi, M. Krakowski and R. Blondeau, Ibid., 24, 10, 609 (1988).

7. W.T. Tsang, N.A. Olsson, R.A. Logan, C.H. Henry, L.F. Johnson, J.E. Bowers and J. Long, IEEE J. QUANTUM ELECTRON, QE-21, 6, 519 (1985).

8. H. Burkhard, E. Kuphal and H.W. Dinges, ELECTRON LETT, Vol 22, 15, 802 (1986).

9. I.P. Kaminow, R.E. Nahory, M.A. Pollack, L.W. Stulz and J.C. Dewinter, ELECTRON LETT., 15, 23, 763 (1979).

10. Wang Wei, Zhang Jingyuan, Tian Huiliang and Sun Furong [1327 1381 2837], YINGYONG JIGUANG [APPLIED LASER TECHNOLOGY], 3, 6, 38 (1983).

11. Zheng Yuhong [6774 5148 4767], Miao Yubo, Tian Huiliang, Yao Yuancheng [1202 5357 ????] and Zhang Jingyuan, BANDAOTI XUEBAO [CHINESE JOURNAL OF SEMICONDUCTORS], 9, 3, 305 (1988).

12. H. Burkhard, IEE PROC. J. OPTOELECTRONICS, 134, 1, 7 (1987).

13. C.Y. Yue, J.D. Peng, Y.B. Liao and B.K. Zhou, ELECTRON LETT., 24, 10, 622 (1988).

GaAs/GaAlAs GRINSCH SQW Phase-Locked Laser Diode Array

90CF0240d Beijing BANDAOTI XUEBAO [CHINESE JOURNAL OF SEMICONDUCTORS] in Chinese Vol 10 No 10, Oct 89 pp 799-804 [MS received 18 Mar 89]

[Article by Zhu Longde [2612 7893 1795] of the Institute of Semiconductors, Chinese Academy of Sciences; G.A.B. Feak and J.M. Ballantyne of the School of Electrical Engineering, Cornell University; and D.K. Wagner and P.L. Tihanyi of the Optoelectronics Center, McDonnell Douglas Astronautics Co.: "A GaAs/GaAlAs Separate-Confinement Single-Quantum-Well Phase-Locked Laser Diode Array]

[Text] **Abstract**

This paper describes a high-power phase-locked laser diode array made of a MOCVD [metallo-organic chemical vapor deposition]-grown separate-confinement single-quantum-well GaAs/GaAlAs wafer. It is an array consisting of 10 single-transverse-mode devices. Its threshold current is 67 mA, its linear power output is greater than 500 mW and its differential quantum efficiency is as high as 60 percent. The array is formed by a strong-coupling and a weak-coupling region. The effect of the strong-coupling region geometry on the coupling mode, i.e., output far-field distribution, was investigated.

Key words: MOCVD, GaAs/GaAlAs, separate-confinement single-quantum-well structure, phase-locked laser diode array, array threshold current, output power, differential quantum efficiency, coupling structure, coupling mode.

I. Introduction

The phase-locked semiconductor laser diode array, conceptually derived from the microwave phased array antenna, has been one of the most studied devices in the past decade.[1-6] The idea is to use an array of laser diodes to raise the light output power. In addition, the oscillating modes of all single-transverse-mode devices are coupled. In order to make sure that there is a fixed spatial and phase relationship among the optical fields of all the devices involved, ideally the phase difference between each oscillation mode should be zero. Thus, it becomes a narrow single-beam high-power device whose beam width is determined by the diffraction limit of the lasing surface linearity of the array. Coherent high-power devices, particularly single-beam high-power phase-locked lasers, have a variety of important promising applications. For example, because they are compact and highly efficient, they make ideal light sources to pump Nd-YAG and Nd-glass lasers if its wavelength can be tuned to 0.807 μm. The output of a coherent high-power laser can be focused to a 2.5-μm diameter spot[7]; by then, the power density can reach 2 mW/cm^2. Therefore, this device can be used in high-data-rate information recording. A single-beam device can also be directly used in point-to-point optical communications in the cosmos and in fiber-optic communications.

Graded-index separate-confinement-heterostructure single-quantum-well (GRINSCH SQW) GaAs/GaAlAs wafers were grown by MOCVD. Broad-contact laser diodes made of these wafers have a threshold current density of 500~1200 A/cm^2. Low-threshold single-transverse-mode laser diodes were fabricated using the chemically assisted ion beam etching (CAIBE) technique.[8] Devices thus made have high yield, good consistency and reproducibility. Hence, they can be used as elements in an array. In a ridge-waveguide phase-locked array with a saturated absorption region, it is possible to obtain an identical-phase coupled-mode (single-beam) laser at a fixed yield.[9] This paper reports the experimental results of a GaAs/GaAlAs GRINSCH SQW ridge-waveguide phase-locked laser diode array in another mode-coupling configuration.

II. Mode-Coupling Configuration of the Array and Device Fabrication

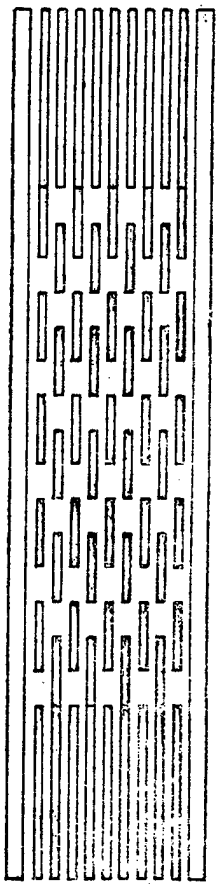

Separate-confinement single-quantum well GaAs/GaAlAs wafers were grown by MOCVD at low pressure (76 torr). The width of a quantum well is 100 Å. The GaAs quantum well is sandwiched between two 0.2-μm thick symmetric undoped waveguide layers with graded index of refraction (aluminum content varies from 0.2 to 0.5).[8] The broad-contact lasing threshold current density of the wafer is 690 A/cm^2 when the cavity is 300 μm long. A ridge waveguide was fabricated using CAIBE.[8] A 2.5-μm stripe-width ridge pattern was etched on the wafer with the array on it. When the etching depth is controlled to 0.2~0.3 μm from the quantum well, excellent refractive transverse waveguide characteristics can be obtained. This means that the curve for light power versus current of the laser is linear within the 20-mW range that was measured. Furthermore, the device has a stable near-field single light-spot distribution.

A phase-coupled laser diode array was made using the ridge-waveguide fabrication technique described above. The array was made of 10 laser diodes spaced 5 μm apart from center to center. The width of each ridge stripe is 2.5 μm. Figure 1 shows the structure of the laser's planar array; in it, the frame represents an etched groove. The array consists of three parts: the 150-μm long region in the middle is the strong-coupling region, or light-mixing region. On each side, there is a 50-μm long full-channel region; these are the weak-coupling regions. They are introduced to stabilize the transverse-mode characteristics of each device.

Figure 1. Coupling Configuration of Ridge-Waveguide Phase-Coupled Laser Diode Array

It consists of a strong-coupling region in the middle and two weak coupling regions, one on each side. In configuration (a), the strong-coupling region in the middle has a 20-μm long trench zone and 10-μm long unetched zone. In configuration (b), both trench and unetched zones are 15 μm in length.

Two configurations have been tested. In configuration (a) the coupling zone between the two ridge waveguides is composed of a 20-μm long trench zone and a 10-μm long unetched area. In configuration (b), the length of the trench region and that of the unetched area are both 15 μm. With a trench, the optical modes are coupled through the overlap of decaying wakes between the stripes. Without a trench, light mixing occurs because it is not limited. The trench area to unetched area length ratio for the strong-coupling region is varied to observe the effects of mixed light intensity and injection between stripes on mode coupling. The modes of the array are isolated by a 5-μm wide trench on either side. A 1400-Å thick SiO_2 film was deposited on the etched array pattern and a 48.75-μm wide electrode stripe window was opened on top of the array. A P-face electrode was made by electron beam evaporation of Ti/Pt/Au. Since it is only possible to form a Schottky contact on exposed GaAlAs, current can only be injected from the unetched side. After trimming one side of the substrate and putting on a Au/Ge/Ni electrode, it was cleaved into stripes according to design.

III. Characteristics of the Laser Diode Array and Analysis

The lasing characteristics of the laser diode array were measured by placing the unsintered cleaved device on a gold-plated copper heat sink with the P side facing up using an 0.5-μs driving current pulse at a 1000-Hz repetition frequency. Results from sintering individual laser diodes showed that the threshold current measured with such a pulse current is less than 10 percent different from that obtained with dc current after sintering. The output characteristics of configurations (a) and (b) are essentially identical, as shown in Figure 2. The devices are fairly consistent. The threshold current is 67 mA. At 1000 mA, the output is 400 mW, and at 1300 mA, the output is over 500 mW. Because the device was not sintered, injection current was not further increased. The external differential quantum efficiency of the device is 60 percent. When the output power of the array is 350 mW, the voltage drop is 2.3 V and the injection current is 880 mA, corresponding to an overall power efficiency of 17 percent. Near-field light distribution was observed with a camera and found to be uniform. Light spots are connected by light that is gradually getting weaker. This illustrates the uniformity of the wafer, the perfection of the device fabrication technique, and consistency of the lasing characteristics of each of the laser diodes in the array. Furthermore, compared to individual laser diodes, the utilization rate of laterally diffusing carriers is higher, resulting in an average threshold current of as low as 6.7 mA and high differential quantum efficiency. The device's power increases linearly up to 300 mW. Above that, although it is somewhat sublinear due to thermal effects, there is still no sign of saturation at 500 mW output and no indication of catastrophic damage. The active region is an 0.1-μm thick double-heterojunction GaAs/GaAlAs laser. The mirror has a catastrophic-damage power limit of 30 mW/2.5-μm wide stripe. Our GRINSCH-structure device has an 0.4-μm thick light-restriction waveguide region. In addition, laterally light is limited by the ridge waveguide. Thus, the optical power density on the mirror is reduced. Therefore, it is reasonable to have a safe output of 50 mW per stripe experimentally. Compared to a broad-contact laser, the laser diode array not only produces a coherent

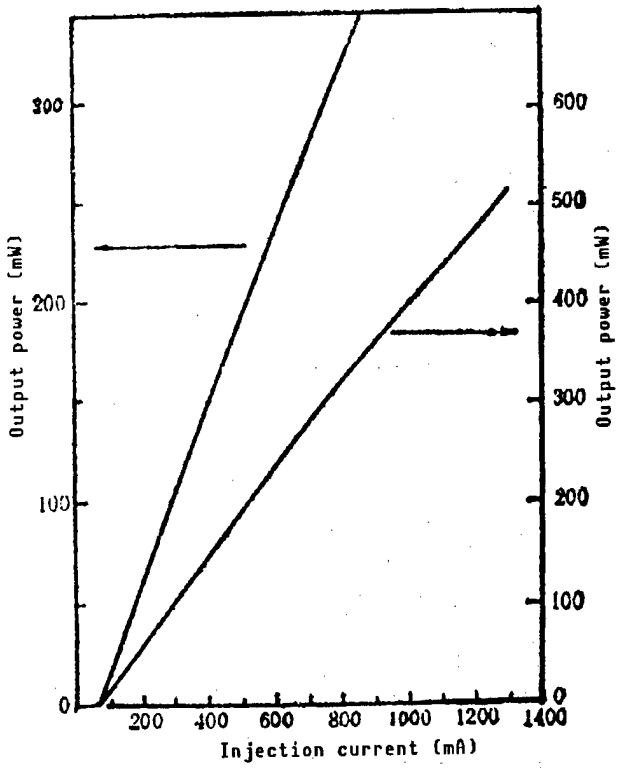

Figure 2. Spatial Coherent Light Output Power of Phase-Coupled Laser Array Vs. Injection Current

optical power but also has a higher safe-power output. This is because it is formed by phase-coupling of relatively independent laser diodes. As long as materials and processes are uniform, light output from the end surface is uniform. A broad-contact laser diode, however, has a higher homogeneity requirement. If materials and electrodes are slightly nonuniform, it results in uneven injection and lasing, and possibly local premature catastrophic failure. Moreover, interaction between the light field and injection carriers results in a spatially unstable incoherent filament. Even though the light emitted appears to be uniform, its far-field width is greater than its diffraction limit and cannot be focused to a small spot with an optical system.

The far-field distribution parallel to the junction plane of the laser diode array is shown in Figure 3. It reflects the actual coupling mode of the oscillating array. Figure 3(a) shows the emission distribution of a device in array configuration (a). We can see that the device emits a single peak up to 1.4 times threshold current. Its half-height width is 2.5 degrees and its power is 14 mW. The diffraction-limited beam width of a coherent emission line element with $\mathcal{L}$ = 48.5 μm is

$$2\theta_h = \frac{2\lambda}{\pi \mathcal{L}} = 0.65^\circ$$

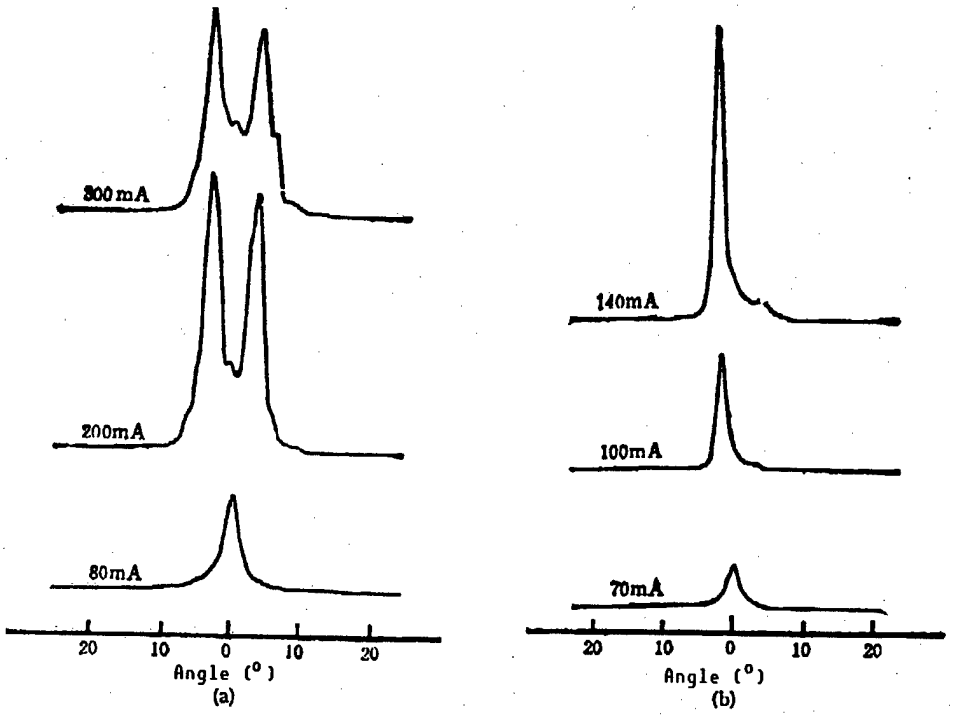

Figure 3. Far-Field Emission-Angle Distribution of Phase-Coupled Laser Diode Array

The half-height width of the emission peak of the array can be calculated using diffraction theory. When the phase difference between adjacent stripes $\varphi = 0$ and there is only a single peak, it is 0.4 degree.[4] This indicates the fact that although there is only a single emission peak, its half width is 4~6 times larger than the theoretical limit. This is probably due to the fact that certain operating parameters such as transient temperature is the active region and current distribution do not remain constant during pulsing. Of course, we cannot eliminate the possibility of having higher-order modes of the array participating in the action. When current was increased to 200 mA, the far-field distribution became two beams, separated by 7 degrees. However, the degree of separation calculated according to diffraction theory is

$$2\theta_{max}=2\tan^{-1}\left(\frac{\lambda}{2D}\right)=9.0^{\circ}$$

where D is the center-to-center spacing between stripes. This calculation is in good agreement with theory which suggests that the $\varphi = \pi$ coupling mode is dominating. When current was increased to 300 mA, the waveform is primarily a superposition of four peaks, indicating more higher-order modes are excited.

In configuration (b) the laser remained with a single-peak output until twice threshold value. The single-peak power could reach 35 mW and the half-power width is 1.3 degrees. It is even narrower than that of configuration (a) and is closer to theoretical values, as shown in Figure 3(b). When current continued to increase, the original peak remained to be the primary peak. An asymmetric side peak appeared on one side. This might be due to the probe

contacting one side of the array, causing nonuniform injection at high current. Since the CAIBE ridge waveguide is ideally square,[8] the electrode is very thin at the corners. In summary, it is easier to attain array fundamental-mode oscillation with $\varphi = 0$ using array configuration (b) than it is with (a). This suggests that it is easier to achieve zero phase coupling among individual oscillation modes by raising the unetched-to-etched-region length ratio in the strong-coupling area. It is not hard to understand this experimental fact. In the strong-coupling region, in addition to overlapping coupling of wakes of various decaying transmission modes (in the trench region), there is very intense diffraction coupling in the unetched region. Besides, increasing the average gain in the region between stripes will suppress the $\varphi = \pi$ inverse phase coupling mode of the array.

IV. Conclusions

GRINSCH SQW GaAs/GaAlAs wafers were prepared by MOCVD. Afterward, ridge-waveguide phase-coupled high-power laser diode arrays were made by CAIBE. The threshold current of the device is 67 mA, the power output is greater than 500 mW, the external differential quantum efficiency is 60 percent, and the overall power efficiency is 17 percent. The output is linear. The array lased a single beam at low current. Configurations with a strong-coupling center and weak-coupling mirror were tested. It was found that a higher unetched-region-to-trench-region length ratio favors zero phase coupling of the fundamental oscillation mode of the array.

Acknowledgement: This work was supported by the Optoelectronics Center of McDonnell Douglas Astronautics Co.

References

1. D.R. Scifres, W. Streifer and R.D. Burnham, APPL. PHYS. LETT., 34, 259 (1979).

2. D.R. Scifres, C. Lindström, R.D. Burnham, W. Streifer and T.L. Paoli, ELECTRON. LETT., 19, 169 (1983).

3. J.V. Ziel, R.M. Mikulyak, H. Temkin, R.A. Logan and R. Dupuis, IEEE J. QUANT. ELECTRON., QE-20, 1259 (1984).

4. D.R. Scifres, W. Streifer and D.R. Burnham, Ibid., QE-15, 917 (199).

5. E. Kapon, J. Katz and A. Yariv, OPTICS LETT., 9, 25 (1984).

6. J.K. Butler, D.E. Ackley and D. Botez, APPL. PHYS. LETT., Vol 44, 293 (1984).

7. D.R. Scifres, R.A. Sprague, W. Streifer and R.D. Burnham, Ibid., 41, 1121 (1982).

8. L.D. Zhu, G.A.B. Feak, R.J. Davis and J.M. Ballantyne, IEEE J. QUANT. ELECTRON., QE-23, 309 (1987).

9. L.D. Zhu, G.A.B. Feak and J.M. Ballantyne, D.K. Wagner and Peter Tihanyi, APPL. PHYS. LETT., 50, 1550 (1987).

GaAs/GaAlAs MQW Structures, Exciton Absorption Spectra

90CF0240e Beijing BANDAOTI XUEBAO [CHINESE JOURNAL OF SEMICONDUCTORS] in Chinese Vol 10 No 11, Nov 89 pp 881-884 [MS Received 27 Sep 88]

[Article by Zeng An [2582 1344], Wu Ronghan [0702 2837 3352], Zeng Yiping [2587 0001 1627], Kong Meiying and Wang Qiming of the Institute of Semiconductors, Chinese Academy of Sciences: "Exciton Absorption Spectra of Multiple-Quantum-Well GaAs/GaAlAs Structures"]

[Text] **Abstract**

The exciton absorption spectra of GaAs/GaAlAs multiple-quantum-well (MQW) structures were measured over a temperature range from 10 K to 292 K. The exciton absorption peaks corresponding to light holes and heavy holes (LH and HH) and a stepwise density of states have been observed. The energy differences of light-hole and heavy-hole exciton absorption peaks and the temperature characteristics of these exciton absorption peaks are studied. The LO phonon broadening coefficient of the MQW samples was found to be 6.1 meV, which is slightly lower than that in bulk GaAs. The specimens were grown in a Chinese-made MBE [molecular beam epitaxy] device and the GaAs substrate was removed by a selective chemical etching technique.

Key words: Multiple quantum well, exciton, absorption spectrum.

Research on semiconductor superlattices and MQWs has been very active in recent years. The superlattice and the quantum well are ideal models for studying lower-dimensional physics and quantum scale effects. The devices also have a bright future. For example, room-temperature optically bistable devices and logic devices[1,2] have been developed by using the room-temperature exciton-saturated absorption characteristics of GaAs/GaAlAs MQW materials. Study shows that exciton absorption usually occurs at low temperatures in bulk GaAs. The GaAs/GaAlAs MQW structure extends the low-temperature exciton characteristics of bulk GaAs to room temperature.[3] Therefore, the study of MQW exciton characteristics is critical to the fabrication of room-temperature optically bistable devices and logic devices. Recently, a wide range of theoretical and experimental studies has been carried out on superlattice MQWs in China. Most experiments are measuring low-temperature fluorescence. The room-temperature and low-temperature characteristics of MQWs and superlattices are rarely studied. Measurement of absorption spectra of GaAs/GaAlAs MQWs and superlattices has not been reported elsewhere.

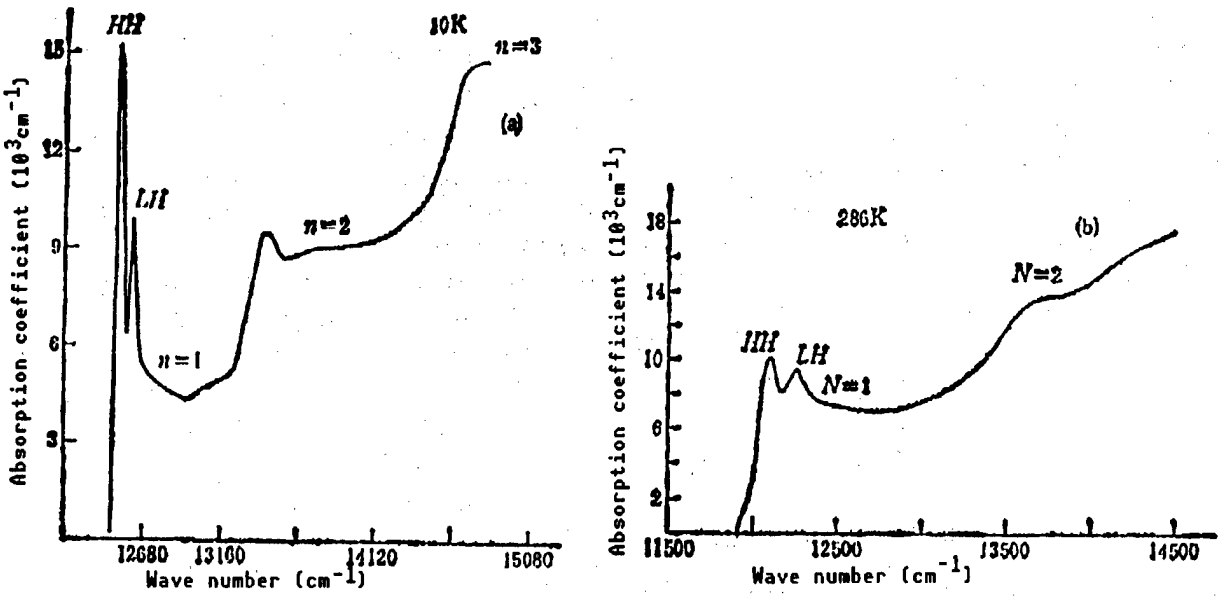

Figure 1. Exciton Absorption Spectra of MQW Structure
(a) Specimen 1, L_x = 100 Å, L_b = 110 Å, cycle T = 120;
(b) Specimen 2, L_x = 67 Å, L_b = 120 Å, x = 0.3, cycle T = 120. LH and HH represent light hole and heavy hole. Specimens are not intentionally doped.

We measured the absorption spectra of MQW specimens grown in our own MBE equipment from low to room temperature. Figure 1 shows the absorption spectra of specimens 1 and 2 at 10 K and at room temperature. Figure 1(a) clearly shows the unique stepwise density of states for a quantum well structure and the exciton absorption peaks corresponding to the n = 1 and n = 2 subbands. The n = 1 subband has very strong exciton absorption and the absorption peak is very narrow. Exciton absorption is weaker in the n = 2 subband and the absorption peak is wider. The exciton absorption corresponding to the n = 3 subband was not observed. This might be due to increasing wave-function iteration as the energy level in the quantum goes up with increasing n. The energy level broadens, which widens the exciton absorption peak and weakens absorption. Figure 1(b) only shows exciton absorption in the n = 1 subband. This is because the well width of specimen 2 is narrower than that of specimen 1. The two absorption peaks associated with the n = 1 subband correspond to the heavy-hole exciton and the light-hole exciton, respectively. The energy difference is $\Delta E_{lh\text{-}hh}^{ex}=\Delta E_{lh\text{-}hh}-\Delta E_{lh\text{-}hh}^{exB}$. $\Delta E_{lh\text{-}hh}$ is the energy-level difference between the light exciton and heavy exciton. $\Delta E_{lh\text{-}hh}^{exB}$ is the binding-energy difference between the light and heavy-hole excitons. From reference 4 we know that $\Delta E_{lh\text{-}hh}^{exB} < 1$ meV. Hence, the energy difference between the light-hole exciton absorption peak and heavy-hole exciton peak, i.e., $\Delta E_{lh\text{-}hh}^{ex}$, is mainly determined by the energy-level difference $\Delta E_{lh\text{-}hh}$ between the light hole and the heavy hole. From quantum theory, $\Delta E_{lh\text{-}hh}$ is dependent upon well width L_x and Al content X. Within a certain range, the narrower and the deeper a well is,

the larger $\Delta E_{lh\text{-}hh}$ becomes. It was measured that $\Delta E^{ex}_{lh\text{-}hh}$ = 10.4 meV for specimen 1, and $\Delta E^{ex}_{lh\text{-}hh}$ = 18.3 meV for specimen 2. These values are consistent with theoretical computations.

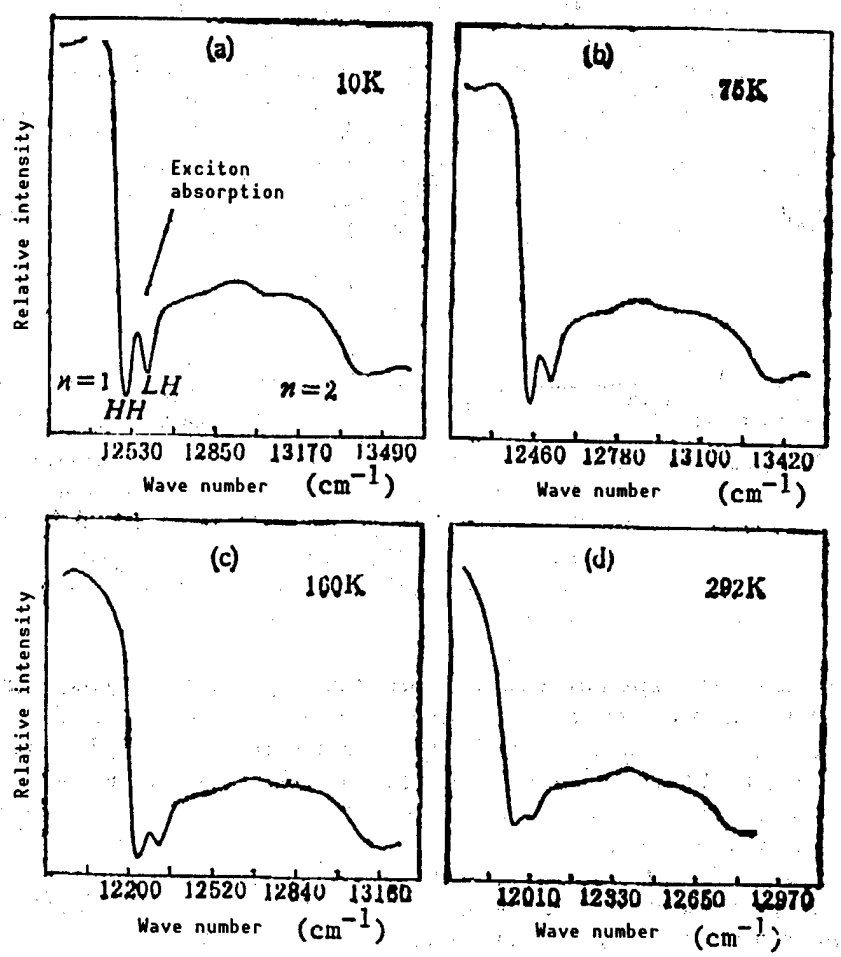

Figure 2. Transmission Spectra of MQW Specimens at (a) 10 K, (b) 75 K, (c) 160 K, and (d) 292 K

Figure 2 shows the transmission spectra of specimen 1 at 10 K, 75 K, 160 K and 292 K. (The transform relation between transmission spectrum and absorption spectrum is $\alpha=\frac{1}{L}\ln\frac{I_{in}}{I_{out}}$. The figure clearly shows that the absorption peak gradually widens with rising temperature and that absorbance decreases. Nevertheless, exciton absorption remains until room temperature. The table below shows how the ratio between the heavy-hole absorption coefficient α_{ex} and the n = 1 subband absorption coefficient α_{1B} varies with temperature. From the table it can be seen that α_{ex}/α_{1B} declines noticeably with increasing temperature because thermal motion dissociates some excitons. In spite of this, the exciton absorption coefficient is still substantial at room temperature: α_{ex} is approximately 1.02 x $10^4 cm^{-1}$.

[T a b l e]

T	10 K	75 K	160 K	292 K
α_{ex}/α_{1B}	3.54	3.34	2.65	1.82

We also studied the dependence of F, i.e., the HWHM (half-width half-maximum) of the heavy-hole exciton absorption peak, upon temperature. F consists of two parts. One part is nonuniform broadening F_0, which does not vary with temperature. It is primarily caused by fluctuation of well width. As a first-order approximation, the half peak width of the spectral line is obtained by differentiating the energy Eigen function of a one-dimensional infinitely deep square well with respect to L_z:

$$\Delta E=2E\frac{\Delta L_z}{L_z^3} \text{ or } \Delta E\propto\frac{\Delta L_z}{L_z^3}$$

F_0 can be obtained experimentally because thermal broadening can be neglected at a low temperature (10 K). The HWHM thus measured is F_0. The absorption spectra and the photoluminescence experiment showed that the values for F_0 in sample 1 are 2.67 meV and 2.65 meV, which are in good agreement. The other part is thermal broadening which increases with rising temperature. We know that the exciton line broadening in GaAs is caused by interaction between exciton and the LO phonon. Because GaAs and GaAlAs have very similar lattice vibration characteristics, the thermal broadening of the exciton line in a MQW should be analogous to that in bulk GaAs, primarily from LO phonons. It is considered that thermal broadening of the exciton line is proportional to LO phonon concentration. Exciton line broadening contains two parts, i.e., nonuniform broadening and thermal broadening:

$$F=F_0+F_B/[\exp]\hbar\omega_{LO}/KT)-1]$$

where $\hbar\omega_{LO}$ is the energy of the LO phonon. F_B is the LO phonon broadening constant. Let us choose a GaAs LO phonon energy $\hbar\omega_{LO}$ = 36 meV, F_0 = 2.67 meV, and F_B = 6.1 meV. We can fit the experimental results well with the above equation, as shown by the solid line in Figure 3. The LO phonon broadening coefficient F_B = 6.1 meV is slightly larger than the value 5.5 meV reported in reference 5. However, it is less than the 7 meV value for GaAs. The GaAs MQW structure increases the exciton binding energy, but reduces its thermal broadening coefficient; this is why exciton absorption is still present at room temperature in MQW structures.

The authors wish to thank Liang Jiben [2733 1015 2609], Sun Dianzhao, Ge Weikun [5514 1919 6924], Xu Zhongying [1776 0112 5391] and Xu Jizong [6079 4949 1350] for their assistance and beneficial discussion.

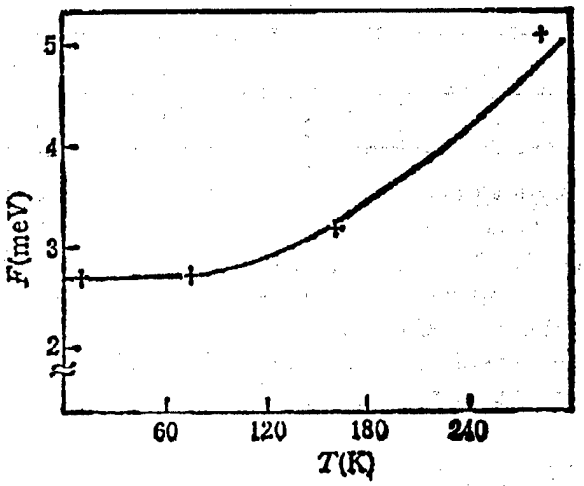

Figure 3. HWHM F of HH Exciton Absorption Peak Vs Temperature T "+" indicates experimental point, solid line is a fitted curve.

References

1. H.M. Gibbs, APPL. PHYS. LETT., 41(3), 221 (1982).

2. D.A.B. Miller, J. OPT. SOC. AM., B1, 857 (1984).

3. D.A.B. Miller, et al., APPL. PHYS., 96 B28, (1982).

4. Ronald L. Greene, SOLID STATE COMMUNICATIONS, 45, 831 (1983).

5. D.S. Chemla, et al., IEEE J. QUANTUM ELECTRON, QE-20, 265 (1984).

6. R. Dingle, In Proc. of 13th Int. Conf. on Phys. of Semiconductors, North-Holland, Amsterdam, 965 (1976).

END

TO

22161
63
NTIS
ATTN: PROCESS 103
5285 PORT ROYAL RD
SPRINGFIELD, VA 22161

Foreign Broadcast Information Service (FBIS) and Joint Publications Research Service (JPRS) publications contain political, economic, military, and sociological news, commentary, and other information, as well as scientific and technical data and reports. All information has been obtained from foreign radio and television broadcasts, news agency transmissions, newspapers, books, and periodicals. Items generally are processed from the first or best available source; it should not be inferred that they have been disseminated only in the medium, in the language, or to the area indicated. Items from foreign language sources are translated; those from English-language sources are transcribed, with personal and place names rendered in accordance with FBIS transliteration style.

Headlines, editorial reports, and material enclosed in brackets [ ] are supplied by FBIS/JPRS. Processing indicators such as [Text] or [Excerpts] in the first line of each item indicate how the information was processed from the original. Unfamiliar names rendered phonetically are enclosed in parentheses. Words or names preceded by a question mark and enclosed in parentheses were not clear from the original source but have been supplied as appropriate to the context. Other unattributed parenthetical notes within the body of an item originate with the source. Times within items are as given by the source. Passages in boldface or italics are as published.

SUBSCRIPTION/PROCUREMENT INFORMATION

The FBIS DAILY REPORT contains current news and information and is published Monday through Friday in eight volumes: China, East Europe, Soviet Union, East Asia, Near East & South Asia, Sub-Saharan Africa, Latin America, and West Europe. Supplements to the DAILY REPORTs may also be available periodically and will be distributed to regular DAILY REPORT subscribers. JPRS publications, which include approximately 50 regional, worldwide, and topical reports, generally contain less time-sensitive information and are published periodically.

Current DAILY REPORTs and JPRS publications are listed in *Government Reports Announcements* issued semimonthly by the National Technical Information Service (NTIS), 5285 Port Royal Road, Springfield, Virginia 22161 and the *Monthly Catalog of U.S. Government Publications* issued by the Superintendent of Documents, U.S. Government Printing Office, Washington, D.C. 20402.

The public may subscribe to either hardcover or microfiche versions of the DAILY REPORTs and JPRS publications through NTIS at the above address or by calling (703) 487-4630 Subscription rates will be provided by NTIS upon request. Subscriptions are available outside the United States from NTIS or appointed foreign dealers. New subscribers should expect a 30-day delay in receipt of the first issue.

U.S. Government offices may obtain subscriptions to the DAILY REPORTs or JPRS publications (hardcover or microfiche) at no charge through their sponsoring organizations. For additional information or assistance, call FBIS, (202) 338-6735,or write to P.O. Box 2604, Washington, D.C. 20013. Department of Defense consumers are required to submit requests through appropriate command validation channels to DIA, RTS-2C, Washington, D.C. 20301. (Telephone: (202) 373-3771, Autovon: 243-3771.)

Back issues or single copies of the DAILY REPORTs and JPRS publications are not available. Both the DAILY REPORTs and the JPRS publications are on file for public reference at the Library of Congress and at many Federal Depository Libraries. Reference copies may also be seen at many public and university libraries throughout the United States.